JOURNAL OF GEOPHYSICAL RESEARCH, VOL. 111, E12S15, doi:10.1029/2006JE002791, 2006

Mössbauer mineralogy of rock, soil, and dust at Meridiani Planum, Mars: Opportunity's journey across sulfate-rich outcrop, basaltic sand and dust, and hematite lag deposits

R. V. Morris,[1] G. Klingelhöfer,[2] C. Schröder,[2] D. S. Rodionov,[2,3] A. Yen,[4] D. W. Ming,[1] P. A. de Souza Jr.,[2,5] T. Wdowiak,[6] I. Fleischer,[2] R. Gellert,[7] B. Bernhardt,[2] U. Bonnes,[8] B. A. Cohen,[9] E. N. Evlanov,[3] J. Foh,[2,8] P. Gütlich,[2] E. Kankeleit,[8] T. McCoy,[10] D. W. Mittlefehldt,[1] F. Renz,[2] M. E. Schmidt,[10] B. Zubkov,[3] S. W. Squyres,[11] and R. E. Arvidson[12]

Received 13 July 2006; revised 4 October 2006; accepted 9 November 2006; published 30 December 2006.

[1] The Mössbauer (MB) spectrometer on Opportunity measured the Fe oxidation state, identified Fe-bearing phases, and measured relative abundances of Fe among those phases at Meridiani Planum, Mars. Eight Fe-bearing phases were identified: jarosite $(K,Na,H_3O)(Fe,Al)(OH)_6(SO_4)_2$, hematite, olivine, pyroxene, magnetite, nanophase ferric oxides (npOx), an unassigned ferric phase, and metallic Fe (kamacite). Burns Formation outcrop rocks consist of hematite-rich spherules dispersed throughout S-rich rock that has nearly constant proportions of Fe^{3+} from jarosite, hematite, and npOx (29%, 36%, and 20% of total Fe). The high oxidation state of the S-rich rock ($Fe^{3+}/Fe_T \sim 0.9$) implies that S is present as the sulfate anion. Jarosite is mineralogical evidence for aqueous processes under acid-sulfate conditions because it has structural hydroxide and sulfate and it forms at low pH. Hematite-rich spherules, eroded from the outcrop, and their fragments are concentrated as hematite-rich soils (lag deposits) on ripple crests (up to 68% of total Fe from hematite). Olivine, pyroxene, and magnetite are primarily associated with basaltic soils and are present as thin and locally discontinuous cover over outcrop rocks, commonly forming aeolian bedforms. Basaltic soils are more reduced ($Fe^{3+}/Fe_T \sim 0.2-0.4$), with the fine-grained and bright aeolian deposits being the most oxidized. Average proportions of total Fe from olivine, pyroxene, npOx, magnetite, and hematite are ~33%, 38%, 18%, 6%, and 4%, respectively. The MB parameters of outcrop npOx and basaltic-soil npOx are different, but it is not possible to infer mineralogical information beyond octahedrally coordinated Fe^{3+}. Basaltic soils at Meridiani Planum and Gusev crater have similar Fe-mineralogical compositions.

Citation: Morris, R. V., et al. (2006), Mössbauer mineralogy of rock, soil, and dust at Meridiani Planum, Mars: Opportunity's journey across sulfate-rich outcrop, basaltic sand and dust, and hematite lag deposits, *J. Geophys. Res.*, *111*, E12S15, doi:10.1029/2006JE002791.

1. Introduction

[2] The Mars Exploration Rover (MER) Opportunity landed in Eagle crater (~20 m diameter) on the low-albedo Noachian-age plains of Meridiani Planum at 1.9483°S, 354.4742°E in International Astronomical Union 2000 coordinates on 24 January 2004 UTC [*Squyres et al.*, 2004]. The primary scientific objective of the exploration of Opportunity and its twin rover Spirit on the opposite side of the planet is to characterize the surface and atmosphere,

[1]NASA Johnson Space Center, Houston, Texas, USA.
[2]Institut für Anorganische und Analytische Chemie, Johannes Gutenberg-Universität, Mainz, Germany.
[3]Space Research Institute IKI, Moscow, Russia.
[4]Jet Propulsion Laboratory, California Institute of Technology, Pasadena, California, USA.
[5]CVRD Group, Rio de Janeiro, Brazil.
[6]Department of Physics, University of Alabama at Birmingham, Birmingham, Alabama, USA.
[7]Department of Physics, University of Guelph, Guelph, Ontario, Canada.
[8]Darmstadt University of Technology, Darmstadt, Germany.
[9]Institute of Meteoritics, University of New Mexico, Albuquerque, NM, USA.
[10]Department of Mineral Sciences, National Museum of Natural History, Smithsonian Institution, Washington, DC, USA.
[11]Department of Astronomy, Cornell University, Ithaca, New York, USA.
[12]Department Earth and Planetary Sciences, Washington University, St. Louis, Missouri, USA.

0148-0227/06/2006JE002791$09.00

searching for evidence of water and clues for assessing past and current climates and their suitability for life [*Squyres et al.*, 2004]. In addition to a miniature Mössbauer (MB) spectrometer (MIMOS II), the Athena science payload on both MER rovers includes a panoramic, multispectral camera (Pancam), a miniature thermal emission spectrometer (MiniTES), an Alpha Particle X-ray spectrometer (APXS), a Microscopic Imager (MI), and a Rock Abrasion Tool (RAT) [*Squyres et al.*, 2003; *Klingelhöfer et al.*, 2003]. The in situ instruments (MB, APXS, MI, and RAT) are mounted on a 5-degree-of-freedom robotic arm for placing the instruments in contact with surface targets.

[3] The MB spectrometer determines the oxidation and coordination states of Fe, the mineralogical composition of Fe-bearing phases, and the distribution of Fe among oxidation and coordination states and Fe-bearing phases. During the first 510 sols (1 sol = 1 Martian day) at Gusev crater, Spirit's MB instrument found both weakly altered and pervasively altered basaltic materials during its journey across the Gusev plains and into the West Spur and Husband Hill regions of the Columbia Hills [*Morris et al.*, 2006]. The weakly altered Adirondack Class basaltic rocks ($Fe^{3+}/Fe_T < 0.2$, $A_{Ol} + A_{Px} \sim 90\%$, and $A_{Ol} \gtrsim A_{Px} > A_{Mt} > A_{Hm}$) are predominant on the Gusev plains. The parameters A_{Ol}, A_{Px}, A_{Mt}, and A_{Hm} are the percentages of total Fe (Fe_T) associated with olivine (Ol), pyroxene (Px), magnetite (Mt), and hematite (Hm). They are derived from the component subspectral areas (*f*-factor corrected [e.g., *De Grave and Van Alboom*, 1991; *Morris et al.*, 1995]). Although weakly altered basaltic float rocks are present in the Columbia Hills (e.g., Backstay Class), moderately to pervasively altered outcrop rocks ($Fe^{3+}/Fe_T = 0.4–0.9$) are widespread in the Columbia Hills. Typically, the altered basaltic rocks have $A_{Ol} + A_{Px} \sim 9–50\%$ and $A_{Px} > A_{Ol}$ ($A_{Ol} \sim 0$ for some rocks like Clovis Class). The major Fe^{3+}-bearing phases are nanophase ferric oxide (npOx), hematite, and goethite (Gt). Goethite (α-FeOOH), whose concentration is highest in the rock Clovis ($A_{Gt} \sim 40\%$), is an important discovery because the phase is mineralogical evidence for aqueous processes as it has structural hydroxide and is formed under aqueous conditions. Ilmenite is also present ($A_{Ilm} \sim 2–8\%$) in some Columbia Hill rocks. Relatively unaltered ($Fe^{3+}/Fe_T \sim 0.3$) basaltic soils (Laguna Class) occur throughout the Gusev plains and the Columbia Hills ($A_{Ol} + A_{Px} \sim 60–80\%$, $A_{npOx} \sim 13–28\%$, and $A_{Mt} \sim 0–10\%$). Highly oxidized ($Fe^{3+}/Fe_T \sim 0.9$), sulfate-rich soils (Paso Robles Class) occur on the Northwest slope of Husband Hill ($A_{Fe(3+)\text{-}Sulfate} \sim 60–90\%$ and $A_{Hm} \sim 0–20\%$).

[4] Preliminary results from Opportunity's Mössbauer spectrometer are reported by *Klingelhöfer et al.* [2004] as part of a special journal issue on the results of the primary mission (first 90 sols). We report here results for the first 560 sols of Opportunity's exploration of Meridiani Planum, which includes the interior and rim of Eagle crater (sols 0–60), the plains eastward to Endurance crater (sols 60–100), the rim and interior of Endurance crater (sols 100–310), and the plains southward to the north of Erebus crater (sols 310–557). *Squyres et al.* [2006b] and *Arvidson et al.* [2006] provide a summary of mission operations and payload measurement campaigns for Opportunity through sol 557 and a summary of key scientific findings derived from all Athena payload elements.

2. Instrument, Measurement, and Spectral Analysis

2.1. Instrument and Measurement

[5] The MER MIMOS II Mössbauer spectrometers have been previously described [*Klingelhöfer et al.*, 2003; *Morris et al.*, 2006]. Briefly, Opportunity's spectrometer operates in backscatter geometry with 512 data channels (triangular waveform at a drive frequency of ~24 Hz, standard but selectable velocity range of ±12 mm/s, and binning of data into 13 temperature windows) and has a primary ^{57}Co radiation source (~300 mCi at launch and ~30 mCi on sol 557) with four detectors to detect resonantly scattered X-rays (6.4 keV) and γ-rays (14.4 keV) from surface targets. Both 6.4 and 14.4 keV data were returned to the Earth because the detector counters were configured to sum, pairwise, counts from the 6.4 and 14.4 keV energy windows. Only 14.4 keV data are discussed in this paper. A secondary radiation source mounted at the opposite end of the velocity transducer plus a known reference absorber (metallic Fe foil, hematite, and magnetite) and detector in transmission geometry are used for velocity calibration during MB operations on the Martian surface. The velocity scale was determined for each temperature window from the reference absorber peak positions, principally those of metallic Fe, and the drive error signal. Opportunity's velocity transducer was less linear compared to the Spirit instrument, and there were often differences in sol-to-sol velocity calibrations.

[6] The robotic arm is used to position MIMOS II into physical contact with surface targets, with contact being sensed by two micro switches on opposite sides of a spring-loaded contact plate. A force of ~1 N or more will close the contact switches. The incident 14.4 keV ^{57}Co gamma radiation illuminates a target area ~1.5 cm in diameter, and the sampling depth is ~0.03 g/cm^2. Temperature sensors on the contact plate and at a location near the reference absorber normally record the same temperature to within ±10 K.

2.2. Mössbauer Spectral Analysis

[7] The Mössbauer parameters for component subspectra that are relevant for oxidation state, coordination state, and phase identification, and distributions thereof are the isomer (or center) shift (δ in mm/s), quadrupole splitting (ΔE_Q in mm/s), magnetic hyperfine field strength (B_{hf} in T, where $B_{hf} = 0$ T for doublets), full peak line width at half maximum intensity (Γ in mm/s), and subspectral areas (A). With respect to phase abundance, subspectral areas provide information about the distribution of total Fe among Fe-bearing phases and do not directly provide information about the distribution of Fe-bearing phases themselves. For example, a sample of Mg_2SiO_4 (Fe-free forsterite) is 100% olivine according to elemental and X-ray diffraction methods, but is 0% olivine according to MB measurements because there is no Fe to detect. We used $\delta = \frac{1}{2}(v_1 + v_2)$ and $\Delta E_Q = |v_2 - v_1|$ for doublet spectra, and $\delta = \frac{1}{4}(v_1 + v_2 + v_5 + v_6)$, $\Delta E_Q = \frac{1}{2}((v_6 - v_5) - (v_2 - v_1))$, and B_{hf} = constant x ($|v_6 - v_1|$) for sextet subspectra, where $v_1, \ldots, v_6$ are the peak center positions in mm/s numbered from

Table 1. Mössbauer Parameters δ, ΔE_Q, and Γ for Fe2D1 (Ol), Fe2D2 (Px), Fe3D1 (npOx), Fe3D4 (Jar), and F3D3 Doublet Subspectra[a]

Generic Name (Assignment)	Fe2D1 (Ol)			Fe2D2 (Px)			Fe3D1 (npOx)			Fe3D3			Fe3D4 (Jar)			
	δ, mm/s	ΔE_Q, mm/s	Γ, mm/s	δ, mm/s	ΔE_Q, mm/s	Γ, mm/s	δ, mm/s	ΔE_Q, mm/s	Γ, mm/s	δ, mm/s	ΔE_Q, mm/s	Γ, mm/s	δ, mm/s	ΔE_Q, mm/s	Γ, mm/s	T, K
Eagle Crater, Meridiani Planum																
B011SU0 (Merlot_Tarmac)[b]	1.15[c]	3.00	0.41	1.14	2.12	0.57	0.37	0.86	0.66	–	–	–	–	–	–	190–280
B016RU0 (StoneMountain_RobertE)	–	–	–	–	–	–	–	–	–	0.37	0.63	0.42	0.37	1.22	0.41	190–260
B017SU0 (BerryFlats_Freckles)	[1.15][d]	[3.00]	[0.41]	[1.14]	[2.12]	[0.57]	[0.37]	[0.85]	[0.66]	–	–	–	–	–	–	250–260
B023SU0 (HematiteSlope_Hema2)	1.15	2.97	0.41	1.13	2.13	0.55	0.41	0.87	0.72	–	–	–	–	–	–	200–280
B025ST2 (BigDig_HemaTrench1)	1.15	3.03	0.39	1.15	2.17	0.59	0.37	0.86	0.77	–	–	–	–	–	–	200–280
B026ST1 (BigDig_HemaTrenchWall2)	1.15	3.02	0.40	1.15	2.13	0.56	0.36	0.89	0.72	–	–	–	–	–	–	200–260
B027RU0 (StoneTablet_Shalt)	[1.15]	[3.00]	[0.41]	[1.14]	[2.12]	[0.57]	–	–	–	[0.37]	[0.60]	[0.39]	[0.36]	[1.20]	[0.46]	240–260
B029RU0 (McKittrick_MiddleRAT)	[1.15]	[3.00]	[0.41]	[1.14]	[2.12]	[0.57]	–	–	–	0.37	0.60	0.39	0.36	1.19	0.39	210–270
B030RU0 (Guadalupe_RATLower)	[1.15]	[3.00]	[0.41]	[1.14]	[2.12]	[0.57]	–	–	–	0.37	0.62	0.45	0.36	1.19	0.47	200–280
B032RR0 (McKittrick_MiddleRAT)	[1.15]	[3.00]	[0.41]	[1.14]	[2.12]	[0.57]	–	–	–	0.37	0.65	0.46	0.36	1.22	0.44	200–270
B035RR0 (Guadalupe_King3)	[1.15]	[3.00]	[0.41]	[1.14]	[2.12]	[0.57]	–	–	–	0.36	0.63	0.41	0.36	1.21	0.49	200–270
B038SU0 (FineSoil_PaydirtPri1)	1.16	3.00	0.40	1.15	2.17	0.59	[0.37]	[0.85]	[0.66]	–	–	–	–	–	–	250–260
B040RU0 (LastChance_Makar)	[1.15]	[3.00]	[0.41]	[1.14]	[2.12]	[0.57]	–	–	–	0.37	0.60	0.47	0.36	1.17	0.47	260–270
B041RU0 (Dells_HiHo)	[1.15]	[3.00]	[0.41]	[1.14]	[2.12]	[0.57]	–	–	–	0.37	0.63	0.52	0.36	1.17	0.52	240–260
B043RU0 (FlatRock_Mojo2)	[1.15]	[3.00]	[0.41]	[1.14]	[2.12]	[0.57]	–	–	–	0.38	0.59	0.38	0.38	1.19	0.38	260–280
B045RR0 (FlatRock_Mojo2)	[1.15]	[3.00]	[0.41]	[1.14]	[2.12]	[0.57]	–	–	–	0.37	0.70	0.47	0.36	1.25	0.40	200–270
B046RU0 (BerryBowl_Empty)	[1.15]	[3.00]	[0.41]	[1.14]	[2.12]	[0.57]	–	–	–	0.39	0.58	0.47	0.38	1.19	0.47	240–270
B048RU0 (BerryBowl_MoessBerry)	[1.15]	[3.00]	[0.41]	[1.14]	[2.12]	[0.57]	0.37	0.91	0.69	–	–	–	–	–	–	200–280
B049RU0 (RasberryNewton_Filling)	[1.15]	[3.00]	[0.41]	[1.14]	[2.12]	[0.57]	–	–	–	0.38	0.62	0.47	0.38	1.19	0.47	240–270
B051RU0 (RealSharksTooth_Enamel1)	[1.15]	[3.00]	[0.41]	[1.14]	[2.12]	[0.57]	–	–	–	0.37	0.64	0.45	0.36	1.19	0.45	200–280
B052SU0 (Goal5WorkVolume_Panaluu)	1.15	3.03	0.39	[1.14]	[2.12]	[0.57]	[0.37]	[0.85]	[0.77]	–	–	–	–	–	–	250–270
B053SU0 (Goal3Field_Vanilla2)	[1.15]	[3.00]	[0.41]	[1.14]	[2.12]	[0.57]	[0.37]	[0.85]	[0.66]	–	–	–	–	–	–	260–270
B054SU0 (MudPie_Coconut2)	[1.15]	[3.00]	[0.41]	[1.14]	[2.12]	[0.57]	[0.37]	[0.85]	[0.66]	–	–	–	–	–	–	240–260
B055SU0 (Meringue_MBone)	[1.15]	[3.00]	[0.41]	[1.14]	[2.12]	[0.57]	[0.37]	[0.85]	[0.66]	–	–	–	–	–	–	230–240
B056SU0 (BlackForest_BriansChoice)	[1.15]	[3.00]	[0.41]	[1.14]	[2.12]	[0.57]	[0.37]	[0.85]	[0.66]	–	–	–	–	–	–	250–260
B060SU0 (MontBlanc_LesHauches)	1.15	3.02	0.41	1.16	2.14	0.59	0.36	0.85	0.73	–	–	–	–	–	–	200–280
Eagle-Endurance Intercrater Plains, Meridiani Planum																
B062SU0 (BlackPatch_Munter)	1.16	3.00	0.38	1.16	2.12	0.54	0.37	0.92	0.74	–	–	–	–	–	–	250–260
B063SU0 (Whitestreak_Cleo3)	[1.15]	[3.03]	[0.39]	[1.15]	[2.17]	[0.59]	[0.37]	[0.85]	[0.77]	–	–	–	–	–	–	250–260
B066RU0 (BounceRock_Glanz2)[e]	–	–	–	1.14	2.22	0.63	–	–	–	–	–	–	–	–	–	200–260
B067RR0 (BounceRock_Case)[e]	–	–	–	1.14	2.21	0.62	–	–	–	–	–	–	–	–	–	200–260
B067RU0 (BounceRock_Eifel)[e]	–	–	–	1.17	2.22	0.67	[0.37]	[0.85]	[0.66]	–	–	–	–	–	–	250–260
B067RU0 (BounceRock_Loreley)[e]	–	–	–	1.15	2.22	0.66	–	–	–	–	–	–	–	–	–	250–260
B068RU0 (BounceRock_Fips2)[e]	–	–	–	1.14	2.22	0.61	–	–	–	–	–	–	–	–	–	200–250
B069RU0 (BounceRock_Grace)[e]	–	–	–	1.15	2.19	0.57	[0.37]	[0.85]	[0.66]	–	–	–	–	–	–	240–260
B069RU0 (BounceRock_Wrigley2)[e]	–	–	–	1.16	2.21	0.61	[0.37]	[0.85]	[0.66]	–	–	–	–	–	–	250–260
B070RU0 (BounceRock_Maggie)[e]	–	–	–	1.13	2.22	0.62	[0.37]	[0.85]	[0.66]	–	–	–	–	–	–	200–210
B073SU0 (Seas_AegeanCrest)	[1.15]	[3.03]	[0.39]	[1.15]	[2.17]	[0.59]	[0.37]	[0.85]	[0.77]	–	–	–	–	–	–	250–270
B078ST1 (DogPark_JeffsChoice)	1.17	2.96	0.41	1.16	2.13	0.55	0.37	0.89	0.73	–	–	–	–	–	–	230–270
B080SU0 (DogPark_JackRussell)	[1.15]	[3.03]	[0.39]	[1.15]	[2.17]	[0.59]	[0.37]	[0.85]	[0.77]	–	–	–	–	–	–	260–270
B084SU0 (Nullarbor_GreatSandy)	[1.15]	[3.03]	[0.39]	[1.15]	[2.17]	[0.59]	[0.37]	[0.85]	[0.77]	–	–	–	–	–	–	250–260
B085RU0 (Baseball_Infield)	[1.15]	[3.00]	[0.41]	[1.15]	[2.17]	[0.59]	–	–	–	0.36	0.65	0.45	0.35	1.17	0.45	240–260
B088RR0 (Pilbara_Golf)	–	–	–	[1.15]	[2.17]	[0.59]	–	–	–	0.36	0.64	0.46	0.36	1.20	0.46	200–260
B090SD0 (PhotoTIDD_Nougat)	1.15	3.01	0.39	1.14	2.14	0.57	0.38	0.84	0.53	–	–	–	–	–	–	200–260
B091RU0 (PhotoTIDD_FredRipple)	[1.15]	[3.03]	[0.39]	[1.15]	[2.17]	[0.59]	[0.37]	[0.85]	[0.77]	–	–	–	–	–	–	250–270
B097SU0 (BerryStop_LeahsChoice)	[1.15]	[3.03]	[0.39]	[1.15]	[2.17]	[0.59]	[0.37]	[0.85]	[0.77]	–	–	–	–	–	–	230–260

Table 1. (continued)

Generic Name (Assignment)	Fe2D1 (Ol)			Fe2D2 (Px)			Fe3D1 (npOx)			Fe3D3			Fe3D4 (Jar)			T, K
	δ, mm/s	ΔE_Q, mm/s	Γ, mm/s	δ, mm/s	ΔE_Q, mm/s	Γ, mm/s	δ, mm/s	ΔE_Q, mm/s	Γ, mm/s	δ, mm/s	ΔE_Q, mm/s	Γ, mm/s	δ, mm/s	ΔE_Q, mm/s	Γ, mm/s	
Endurance Crater, Meridiani Planum																
B105RU0 (LionStone_Nala)	–	–	–	[1.14]	[2.12]	[0.57]	–	–	–	0.36	0.61	0.43	0.36	1.22	0.43	240–260
B108RR0 (LionStone_NummaNewNormal)	[1.15]	[3.00]	[0.41]	[1.14]	[2.12]	[0.57]	–	–	–	0.38	0.64	0.46	0.37	1.19	0.46	250–260
B121RU0 (FigTree_Barberton2)	1.15	3.01	0.40	1.14	2.13	0.53	[0.37]	[0.85]	[0.66]	–	–	–	–	–	–	230–270
B123SU0 (HillTop_McDonnell)	1.16	3.00	0.46	1.15	2.11	0.65	[0.37]	0.80	0.58	–	–	–	–	–	–	240–270
B124RU0 (Pyrrho_Sweet)	[1.15]	[3.00]	[0.41]	[1.14]	[2.12]	[0.57]	–	–	–	0.39	0.59	0.44	0.37	1.20	0.44	250–270
B126RU0 (Diogenes_MyTier02)	[1.15]	[3.00]	[0.41]	[1.14]	[2.12]	[0.57]	–	–	–	0.36	0.64	0.42	0.36	1.20	0.42	230–250
B140RR0 (Tennessee_Vols)	[1.15]	[3.00]	[0.41]	[1.14]	[2.12]	[0.57]	–	–	–	0.38	0.63	0.47	0.37	1.19	0.47	200–250
B142RU0 (Kentucky_BlueGrass2)	[1.15]	[3.00]	[0.41]	[1.14]	[2.12]	[0.57]	–	–	–	0.37	0.58	0.41	0.36	1.17	0.41	250–260
B143RU0 (Kentucky_Churchill)	[1.15]	[3.00]	[0.41]	[1.14]	[2.12]	[0.57]	–	–	–	0.38	0.61	0.44	0.37	1.20	0.44	200–250
B144RR0 (Kentucky_CobbleHill)	[1.15]	[3.00]	[0.41]	[1.14]	[2.12]	[0.57]	–	–	–	0.37	0.63	0.44	0.36	1.21	0.44	200–260
B148RR0 (LayerC_Virginia)	[1.15]	[3.00]	[0.41]	[1.14]	[2.12]	[0.57]	–	–	–	0.38	0.61	0.44	0.37	1.21	0.44	200–260
B150RR0 (Ontario_London)	[1.15]	[3.00]	[0.41]	[1.14]	[2.12]	[0.57]	–	–	–	0.37	0.63	0.43	0.37	1.21	0.43	200–260
B152RR0 (Manitoba_Grindstone)	[1.15]	[3.00]	[0.41]	[1.14]	[2.12]	[0.57]	–	–	–	0.38	0.61	0.43	0.37	1.21	0.43	200–260
B154RR0 (Manitoba_Kettlestone)	[1.15]	[3.00]	[0.41]	[1.14]	[2.12]	[0.57]	–	–	–	0.38	0.59	0.42	0.37	1.20	0.42	200–270
B163RR0 (Millstone_Drammensfjord)	[1.15]	[3.00]	[0.41]	[1.14]	[2.12]	[0.57]	–	–	–	0.37	0.60	0.42	0.36	1.19	0.42	200–260
B165SU0 (Millstone_Dahlia)	1.16	2.99	0.39	1.15	2.12	0.58	0.40	0.86	0.61	–	–	–	–	–	–	210–260
B174RU0 (Hoghead_ArnoldZiffel)	[1.15]	[3.00]	[0.41]	[1.14]	[2.12]	[0.57]	–	–	–	0.37	0.63	0.44	0.37	1.21	0.44	230–240
B179RR0 (DiamondJenness_Holman3)	[1.15]	[3.00]	[0.41]	[1.14]	[2.12]	[0.57]	–	–	–	0.39	0.58	0.43	0.37	1.20	0.43	200–250
B183RR0 (Mackenzie_Campbell2)	[1.15]	[3.00]	[0.41]	[1.14]	[2.12]	[0.57]	–	–	–	0.37	0.59	0.43	0.36	1.19	0.43	220–250
B188RR0 (Inuvik_Tuktoyaktuk)	[1.15]	[3.00]	[0.41]	[1.14]	[2.12]	[0.57]	–	–	–	0.39	0.64	0.46	0.37	1.21	0.46	200–260
B196RR0 (Bylot_Aktineq3)	[1.15]	[3.00]	[0.41]	[1.14]	[2.12]	[0.57]	–	–	–	0.36	0.58	0.57	0.36	1.18	0.57	210–260
B198RU0 (Bylot_Sermilik)	[1.15]	[3.00]	[0.41]	[1.14]	[2.12]	[0.57]	–	–	–	0.39	0.64	0.42	0.38	1.23	0.42	240–260
B211RU0 (Escher_AfarMB)	[1.15]	[3.00]	[0.41]	[1.14]	[2.12]	[0.57]	–	–	–	0.37	0.63	0.51	0.37	1.17	0.51	210–260
B213RU0 (Escher_Kirchner)	[1.15]	[3.00]	[0.41]	[1.14]	[2.12]	[0.57]	–	–	–	0.38	0.65	0.50	0.36	1.20	0.50	210–260
B215RB0 (Escher_Kirchner)	[1.15]	[3.00]	[0.41]	[1.14]	[2.12]	[0.57]	–	–	–	0.37	0.64	0.51	0.36	1.22	0.51	210–260
B217RB0 (Escher_EmilNolde)	[1.15]	[3.00]	[0.41]	[1.14]	[2.12]	[0.57]	–	–	–	0.37	0.65	0.49	0.36	1.18	0.49	210–260
B219RR0 (Escher_Kirchner)	[1.15]	[3.00]	[0.41]	[1.14]	[2.12]	[0.57]	–	–	–	0.37	0.60	0.41	0.37	1.20	0.41	210–270
B222SU0 (BerrySurvey_Cluster3)	[1.15]	[3.03]	[0.39]	[1.15]	[2.17]	[0.59]	[0.37]	[0.85]	[0.77]	–	–	–	–	–	–	200–260
B237SB0 (Auk_AukRAT)	1.15	2.99	0.40	1.15	2.13	0.59	0.38	0.94	0.63	–	–	–	–	–	–	210–260
B241RU0 (Ellesmere_Barbeau3)	[1.15]	[3.00]	[0.41]	[1.15]	[2.17]	[0.59]	–	–	–	0.36	0.61	0.53	0.37	1.16	0.53	210–250
B246SU0 (Rocknest_VoidMod)	1.16	3.00	0.41	1.15	2.13	0.55	0.39	0.90	0.69	–	–	–	–	–	–	190–240
B308RR0 (Blackcow_Wharenhui)	[1.15]	[3.00]	[0.41]	[1.14]	[2.12]	[0.57]	–	–	–	0.36	0.63	0.48	0.36	1.21	0.48	190–270
Endurance-Erebus Intercrater Plains, Meridiani Planum																
B348RU0 (SpongeBob_Squidward)[f]	–	–	–	–	–	–	0.34	0.76	0.44	–	–	–	–	–	–	210–270
B351RB0 (SpongeBob_Squidward)[f]	–	–	–	–	–	–	0.33	0.72	0.52	–	–	–	–	–	–	210–270
B367ST1 (Trench_LeftOfPeanut)	1.15	2.99	0.41	1.16	2.10	0.57	0.37	0.87	0.68	–	–	–	–	–	–	210–280
B368SU0 (TrenchRipple_RippleCrest2b)	[1.15]	[3.03]	[0.39]	[1.15]	[2.17]	[0.59]	[0.37]	[0.85]	[0.77]	–	–	–	–	–	–	250–280
B369SU0 (TrenchRipple_CavairTweaked)	1.14	2.94	0.32	1.18	2.09	0.72	0.37	0.92	0.55	–	–	–	–	–	–	260–280
B373SD0 (Trench_Scruffy)	1.16	2.97	0.41	1.14	2.11	0.65	0.37	0.89	0.56	–	–	–	–	–	–	250–280
B380RU0 (Russett_BridgeOfNose)	–	–	–	[1.14]	[2.12]	[0.57]	–	–	–	0.38	0.63	0.42	0.36	1.20	0.42	250–280
B392RU0 (Normandy_Omaha)	[1.15]	[3.00]	[0.41]	[1.14]	[2.12]	[0.57]	–	–	–	0.37	0.63	0.44	0.38	1.22	0.44	210–280
B404RR0 (Yuri_Gagarin)	[1.15]	[3.00]	[0.41]	[1.14]	[2.12]	[0.57]	–	–	–	0.38	0.64	0.47	0.38	1.22	0.47	210–270
B415SU0 (MattsRipple_Mobarak)	[1.15]	[3.03]	[0.39]	[1.15]	[2.17]	[0.59]	[0.37]	[0.85]	[0.77]	–	–	–	–	–	–	190–270
B419SU0 (Ripple_Norooz)	[1.15]	[3.03]	[0.39]	[1.15]	[2.17]	[0.59]	[0.37]	[0.85]	[0.77]	–	–	–	–	–	–	250–290
B420SU0 (Ripple_Mayberooz)	[1.15]	[3.03]	[0.39]	[1.15]	[2.17]	[0.59]	[0.37]	[0.85]	[0.77]	–	–	–	–	–	–	250–290
B445SD0 (RecoverySoil_Cure)	[1.15]	[3.03]	[0.39]	[1.15]	[2.17]	[0.59]	[0.37]	[0.85]	[0.77]	–	–	–	–	–	–	190–270
B509SD0 (Purgatory_Track2)	1.14	3.02	0.51	1.17	2.15	0.65	0.37	0.90	0.81	–	–	–	–	–	–	190–270

Table 1. (continued)

Generic Name (Assignment)	Fe2D1 (Ol)			Fe2D2 (Px)			Fe3D1 (npOx)			Fe3D3			Fe3D4 (Jar)			T, K
	δ, mm/s	ΔE_Q, mm/s	Γ, mm/s	δ, mm/s	ΔE_Q, mm/s	Γ, mm/s	δ, mm/s	ΔE_Q, mm/s	Γ, mm/s	δ, mm/s	ΔE_Q, mm/s	Γ, mm/s	δ, mm/s	ΔE_Q, mm/s	Γ, mm/s	
B548RR0 (IceCream_Onescoop)	[1.15]	[3.00]	[0.41]	[1.14]	[2.12]	[0.57]	–	–	–	0.39	0.55	0.51	0.38	1.19	0.51	200–270
B551RU0 (Cobbles_Arkansas)	[1.15]	[3.00]	[0.41]	1.17	2.31	0.55	0.34	1.04	0.79	–	–	–	–	–	–	200–270
B557RB0 (FruitBasket_LemonRind)	[1.15]	[2.95]	[0.38]	[1.14]	[2.12]	[0.57]	–	–	–	0.36	0.64	0.54	0.37	1.21	0.54	210–270

[a]Parameters were calculated from spectra summed over the temperature interval given in the last column. The values of δ are referenced to metallic iron foil at the same temperature as the sample.
[b]Target naming convention: Bwwwxyz (Feature-name_Target-name). B, MER-B (Meridiani Planum); www, Meridiani Planum sol number that data product was returned to Earth. For integrations covering multiple sols, the sol of the first returned data product is used. x = R (rock) or S (soil); y = U (undisturbed), D (disturbed), T (trench), B (RAT-brushed surface), R (RAT-ground surface), or G (RAT grindings); z = 0 by default; z = 1, 2, 3. . . for multiple analyses of the same target on the same sol. For BxxxSTz, z = 1, 2, 3. . . with increasing number corresponding to increasing depth. Alphanumeric strings before parentheses are unique target identifiers.
[c]MB parameter errors are ±0.02 mm/s.
[d]Parameters in square brackets were held constant during fitting procedures.
[e]One-doublet fits for Px in BounceRock. For two-doublet fits, average ±1σ values of δ, ΔE_Q, and Γ are 1.14 ± 0.02 mm/s, 2.04 ± 0.03 mm/s, and 0.46 ± 0.02 mm/s, respectively, for one doublet and 1.17 ± 0.02 mm/s, 2.73 ± 0.04 mm/s, and 0.43 ± 0.06 mm/s, respectively, for the other.
[f]Heat Shield rock.

minimum to maximum velocity. With adequate counting statistics, the peak center positions can be obtained using least squares computer programs where, for example, the peak line shape, center, width, and area are adjustable parameters.

[8] On Mars, optimal counting statistics in any given temperature window for a single target are not often achieved because arbitrarily long counting times are not possible. The situation degrades with mission time in accordance with the 270 d half-life of ^{57}Co. We employed two approaches to improve counting statistics [*Morris et al.*, 2006]. One was to sum the MB data for a subset or all of the temperature windows for a single target, and the other was to sum data for the same temperature interval (one or more temperature windows) over multiple targets. In the second case, subspectral areas for individual targets are calculated using previously obtained information (subspectral δ, ΔE_Q, and B_{hf}) as fitting constraints.

[9] A total of five doublet and four sextet subspectra were required to fit the MB spectra of 95 targets analyzed by Opportunity. Generic names will be used for the subspectra, and their assignments to oxidation and coordination state and Fe-bearing phase will be discussed in the next section. The generic subspectral names [after *Morris et al.*, 2006] have the format FeXYZ, where X = 2, 2.5, or 3 according to Fe oxidation state, Y = D or S (doublet or sextet), and Z is a sequential number for subspectra having the same FeXY. Most spectra were independently fit by at least two authors of this paper using different approaches. In one approach, Lorentzian line shapes were assumed, peak parameters were the adjustable parameters (within the constraint guidelines discussed below), and the MB parameters δ, ΔE_Q, and B_{hf} were calculated from the fit peak positions. In the other approach, δ, ΔE_Q, and B_{hf} (and distributions thereof) for each subspectrum were the adjustable parameters. The values of MB parameters that we report for each subspectrum (δ, ΔE_Q, B_{hf}, and A) are the average of our independent fits, and the parameter errors are the larger of the uncertainty of the average value (usually) or the statistical error. Minimum errors we report are ±0.02 mm/s for δ and ΔE_Q, ±0.8 T for B_{hf}, and ±2% (absolute) for A.

[10] With regard to fitting procedures, the component peaks for doublet subspectra were constrained to have equal areas and equal widths. For sextet subspectra, peak areas were constrained to the ratio 3:2:1:1:2:3. The centers of the innermost two sextet peaks, because they have comparatively low intensity and strongly overlap with doublet subspectra, were constrained using the positions of the other four peaks and 0.572 for the *g*-factor ratio of the 14.4 keV excited state to the ground state of ^{57}Fe [e.g., *Gütlich et al.*, 1978], and their values of Γ are constrained equal to values between 0.35 and 0.45 mm/s. Two sextet subspectra (Fe2.5S1 and Fe3S1, which are assigned to the octahedrally and tetrahedrally coordinated sites of magnetite, respectively [*Morris et al.*, 2006]) are not present with sufficient intensity in Meridiani Planum MB spectra to fit without constraining δ, ΔE_Q, B_{hf}, and Γ to initial values and peak areas to the ratio 3:2:1:1:2:3. For the initial values, we used the parameters reported by *Morris et al.* [2006] for Gusev crater magnetite. For Heat Shield Rock, the peak parameters for sextet subspectrum Fe0S1 (assigned to metallic Fe) were not constrained.

Table 2. Mössbauer Parameters δ, ΔE_Q, and B_{hf} for Sextet Subspectra[a]

	δ, mm/s	ΔE_Q, mm/s	B_{hf}, T	T, K
	Fe3S1 (Magnetite, tet-Fe^{3+})[b]			
All Mt-bearing targets	[0.31][c]	[0.06]	[50.1]	
	Fe2.5S1 (Magnetite, oct-$Fe^{2.5+}$)[b]			
All Mt-bearing targets	[0.64]	[0.00]	[46.9]	
	Fe3S2 (Hematite)			
All Laguna Class Soil	[0.37]	[−0.16]	[51.7]	–
B016RU0 (StoneMountain_RobertE)	0.34[d]	−0.01	52.1[d]	190–260
B027RU0 (StoneTablet_Shalt)	[0.36]	[−0.09]	[51.5]	240–260
B029RU0 (McKittrick_MiddleRAT)	0.36	−0.09	51.5	210–270
B030RU0 (Guadalupe_RATLower)	0.36	−0.10	52.3	200–280
B032RR0 (McKittrick_MiddleRAT)	0.35	−0.07	51.5	200–270
B035RR0 (Guadalupe_King3)	0.34	−0.07	52.0	200–270
B040RU0 (LastChance_Makar)	[0.36]	[−0.09]	[51.5]	260–270
B041RU0 (Dells_HiHo)	[0.36]	[−0.09]	[51.5]	240–260
B043RU0 (FlatRock_Mojo2)	[0.37]	[−0.16]	[51.7]	260–280
B045RR0 (FlatRock_Mojo2)	0.33	−0.06	51.9	200–270
B046RU0 (BerryBowl_Empty)	0.36	−0.12	51.6	240–270
B048RU0 (BerryBowl_MoessBerry)	0.38	−0.07	53.1	200–280
B049RU0 (RasberryNewton_Filling)	[0.36]	[−0.09]	[51.5]	240–270
B051RU0 (RealSharksTooth_Enamel1)	0.37	−0.01	52.3	200–280
B052SU0 (Goal5WorkVolume_Panaluu)	0.36	−0.19	52.2	250–270
B073SU0 (Seas_AegeanCrest)	0.37	−0.20	51.9	250–270
B080SU0 (DogPark_JackRussell)	0.35	−0.19	52.5	260–270
B084SU0 (Nullarbor_GreatSandy)	0.37	−0.21	52.3	250–260
B085RU0 (Baseball_Infield)	0.36	−0.09	51.5	240–260
B088RR0 (Pilbara_Golf)	0.33	−0.02	52.5	200–260
B091RU0 (PhotoTIDD_FredRipple)	0.36	−0.19	52.2	250–270
B097SU0 (BerryStop_LeahsChoice)	0.37	−0.12	52.5	230–260
B105RU0 (LionStone_Nala)	0.39	−0.07	52.5	240–260
B108RR0 (LionStone_NummaNewNormal)	[0.36]	[−0.09]	[51.5]	250–260
B124RU0 (Pyrrho_Sweet)	0.34	0.03	52.1	250–270
B126RU0 (Diogenes_MyTier02)	0.35	0.03	51.6	230–250
B140RR0 (Tennessee_Vols)	0.36	0.02	51.8	200–250
B142RU0 (Kentucky_BlueGrass2)	0.34	0.00	50.7	250–260
B143RU0 (Kentucky_Churchill)	0.36	0.03	53.0	200–250
B144RR0 (Kentucky_CobbleHill)	0.36	−0.05	52.1	200–260
B148RR0 (LayerC_Virginia)	0.36	−0.07	52.1	200–260
B150RR0 (Ontario_London)	0.35	−0.08	51.7	200–260
B152RR0 (Manitoba_Grindstone)	0.36	−0.10	51.9	200–260
B154RR0 (Manitoba_Kettlestone)	0.34	−0.05	51.7	200–270
B163RR0 (Millstone_Drammensfjord)	0.33	−0.02	51.5	200–260
B174RU0 (Hoghead_ArnoldZiffel)	0.36	−0.04	52.2	230–240
B179RR0 (DiamondJenness_Holman3)	0.35	−0.01	51.8	200–250
B183RR0 (Mackenzie_Campbell2)	0.33	−0.06	51.7	220–250
B188RR0 (Inuvik_Tuktoyaktuk)	0.35	−0.07	51.5	200–260
B196RR0 (Bylot_Aktineq3)	0.36	−0.03	52.1	210–260
B198RU0 (Bylot_Sermilik)	0.40	−0.04	51.7	240–260
B211RU0 (Escher_AfarMB)	0.36	−0.07	51.8	210–260
B213RU0 (Escher_Kirchner)	0.37	−0.03	52.2	210–260
B215RB0 (Escher_Kirchner)	0.34	−0.06	52.1	210–260
B217RB0 (Escher_EmilNolde)	0.35	−0.03	51.9	210–260
B219RR0 (Escher_Kirchner)	0.37	−0.08	51.9	210–270
B222SU0 (BerrySurvey_Cluster3)	0.37	−0.07	53.2	200–260
B241RU0 (Ellesmere_Barbeau3)	0.36	−0.34	52.1	210–250
B308RR0 (Blackcow_Wharenhui)	0.35	−0.04	52.1	190–270
B368SU0 (TrenchRipple_RippleCrest2b)	0.37	−0.18	51.8	250–280
B380RU0 (Russett_BridgeOfNose)	0.37	−0.06	51.5	250–280
B392RU0 (Normandy_Omaha)	0.38	−0.12	52.1	210–280
B404RR0 (Yuri_Gagarin)	0.37	−0.07	52.3	210–270
B415SU0 (MattsRipple_Mobarak)	0.37	−0.12	52.3	190–270
B419SU0 (Ripple_Norooz)	0.35	−0.21	51.9	250–290
B420SU0 (Ripple_Mayberooz)	0.36	−0.21	51.8	250–290
B445SD0 (RecoverySoil_Cure)	0.36	−0.10	52.7	190–270
B548RR0 (IceCream_Onescoop)	0.35	−0.04	52.2	200–270
B551RU0 (Cobbles_Arkansas)	[0.37]	[−0.08]	[51.9]	200–270
B557RB0 (FruitBasket_LemonRind)	0.36	−0.05	52.3	210–270

Table 2. (continued)

	δ, mm/s	ΔE_Q, mm/s	B_{hf}, T	T, K
	Fe0S1 (α-(Fe^0,Ni^0) Metal Alloy)			
B121RU0 (FigTree_Barberton2)	[0.00]	[0.00]	[34.7]	230–270
B348RU0 (SpongeBob_Squidward)[e]	0.00	0.00	34.7	210–270
B351RB0 (SpongeBob_Squidward)[e]	0.00	0.00	34.6	210–270

[a]Parameters were calculated from spectra summed over the temperature interval given in the last column. Values of δ are with respect to metallic iron foil at the same temperature as the sample.
[b]Parameters from Gusev crater Mt [*Morris et al.*, 2006].
[c]Parameters in square brackets were held constant during fitting procedures.
[d]MB parameter errors are ±0.02 mm/s for δ and ΔE_Q and ±0.8 T for B_{hf}.
[e]Heat Shield rock. MB parameter errors are ±0.02 mm/s for δ and ΔE_Q and ±0.4 T for B_{hf}.

[11] The values of δ, ΔE_Q, and Γ for Fe2D1 (assigned to olivine), Fe2D2 (assigned to pyroxene), Fe3D1 (assigned to npOx), Fe3D3 (unassigned), and Fe3D4 (assigned to jarosite) doublet subspectra were not normally constrained to initial values, except for spectra where counting statistics were poor and/or their subspectral areas were small. For the case of poor counting statistics and the occurrence of Fe3D3 and Fe3D4, the values of δ and ΔE_Q were not constrained but the values of Γ for both doublets were constrained equal. Similarly, the values of δ, ΔE_Q, B_{hf}, and Γ for Fe3S2 (assigned to hematite) were not constrained to initial values unless counting statistics were poor and/or subspectral areas were small.

[12] Derived values of MB parameters δ, ΔE_Q, B_{hf}, and Γ for individual targets are given in Table 1 (doublet subspectra) and Table 2 (sextet subspectra). Values in square brackets were held constant (constrained to initial values) during fitting procedures. The spectra from which the parameters were derived are the sum over the temperature interval given in the last column of each table. Subspectral areas (A) are compiled in Table 3, and they include a correction factor (the *f*-factor) to account for differences in recoil-free fractions ($f(Fe^{3+})/f(Fe^{2+}) = 1.21$) independent of mineralogical composition [*De Grave and Van Alboom*, 1991; *Morris et al.*, 1995]).

3. Phase Identification

3.1. Overview

[13] We use a combination of literature databases of MB parameters [e.g., *Burns and Solberg*, 1990; *McCammon*, 1995; *Stevens et al.*, 1998; *de Souza*, 1999], intercorrelations of subspectral areas, correlation of subspectral areas with APXS elemental data, and mineralogical observations of other MER instruments (MiniTES and Pancam) to make phase assignments [*Morris et al.*, 2006].

[14] Typically, literature databases include MB parameters measured near room temperature (~295 K) and at temperatures well below the diurnal temperature range experienced by the MER rovers (~180–300 K). Important exceptions are iron oxides such as hematite and goethite which have been well studied because they undergo magnetic transitions within (Morin transition of hematite at ~260 K) or near (Verwey transition of magnetite at ~120 K and Neel transition of goethite at ~420 K) Martian diurnal temperatures. *Dyar and Schaefer* [2004] argued that 295 K data cannot be used because the temperature dependence of MB parameters is significant. This is not the case, as discussed next.

[15] In the absence of magnetic transitions, we showed that the MER MB parameters are not significantly temperature dependent, in part because of the way MB measurements are made on Mars and in part because the parameters are not significantly dependent on temperature [*Morris et al.*, 2006]. On Mars, the ^{57}Co source and absorber (i.e., surface target) are nominally at the same temperature (within ±10 K), so that values of δ are referenced to metallic Fe at the sample temperature. In typical laboratory instruments (including *Dyar and Schaefer* [2004]), the instrumental configuration has the source at room temperature and the absorber in a cryostat at lower temperatures. In this case, the values of δ are referenced to metallic Fe at room temperature and significant temperature dependence is observed. Thus direct comparison of literature MB data acquired over the Martian diurnal temperature range involves using literature values of δ at room temperature (because they are obtained with source and absorber at the same temperature) and the low-temperature values of ΔE_Q and B_{hf} if they are temperature dependent. For MB spectra from Gusev crater [*Morris et al.*, 2006], δ and ΔE_Q for doublet subspectra are temperature independent within error, implying that literature values of ΔE_Q measured at room temperature can be directly applied to MER data obtained at diurnal temperatures.

[16] Although the ideal database is one where MB measurements are made at Martian diurnal temperatures with a MER-like configuration where the ^{57}Co source, Fe metal calibration standard, and sample are all at the same temperature, such a database is not required as discussed above. Either the parameters are not significantly temperature dependent (δ and ΔE_Q for doublet subspectra and δ for sextet subspectra) or the temperature dependence is known (ΔE_Q and B_{hf} for sextet subspectra) from previous publications describing the temperature dependence of magnetic transitions. It is also possible that there are Fe-bearing phases on Mars that are unknown in terrestrial samples.

[17] Intercorrelation of subspectral areas and correlation of subspectral areas with elemental data provide additional constraints for phase identifications [*Morris et al.*, 2006]. For example, the negative correlation of A_{npOx} with A_{Px} and the positive correlation of A_{npOx} with SO_3 is evidence that Fe^{3+}-bearing phase is correctly assigned to a weathering product (npOx) and not to Fe^{3+} in pyroxene. Anion-cation charge balance considerations and the exceptionally high S abundance in the Fe^{3+}-rich PasoRobles Class soils are compelling evidence that the Fe^{3+} doublet subspectrum that is unique to the Paso Robles Class is a Fe^{3+}-sulfate. And

Table 3. Mössbauer Areas for Component Subspectra (f-Factor Corrected), Fe^{3+}/Fe_T, and Temperature Measurement Interval for Mössbauer Spectra of Meridiani Planum Rock and Soil Targets

Generic Name / Phase Assignment	Fe2D1 Ol, %	Fe2D2 Px, %	Fe3D1 npOx, %	Fe3D4 Jar, %	Fe3D3 Fe3D3, %	Mt, %	Fe3S1 Mt(3), %	Fe2.5S1 Mt(2.5), %	Fe3S2 Hm, %	Fe0S1 α-(Fe,Ni)^0, %	Sum, %	Fe^{3+}/Fe_T	T, K
Eagle Crater, Meridiani Planum													
B011SU0 (Merlot_Tarmac)	39[a]	37	14	0	0	6[b]	2	4	4[b]	0	100[c]	0.22[d]	190–280
B016RU0 (StoneMountain_RobertE)	4	12	0	26	18	0	0	0	40	0	100	0.84	190–260
B017SU0 (BerryFlats_Freckles)	26	28	10	0	0	0	0	0	35	0	100	0.46	250–260
B023SU0 (HematiteSlope_Hema2)	29	30	13	0	0	6[b]	2	4	22[b]	0	100	0.39	200–280
B025ST2 (BigDig_HemaTrench1)	20	31	39	0	0	5[b]	2	3	6[b]	0	100	0.48	200–280
B026ST1 (BigDig_HemaTrenchWall2)	31	35	22	0	0	5[b]	2	4	7[b]	0	100	0.32	200–260
B027RU0 (StoneTablet_Shalt)	1	12	0	31	19	0	0	0	37	0	100	0.87	240–260
B029RU0 (McKittrick_MiddleRAT)	10	18	0	26	16	0	0	0	31	0	100	0.72	210–270
B030RU0 (Guadalupe_RATLower)	3	9	0	27	17	0	0	0	45	0	100	0.88	200–280
B032RR0 (McKittrick_MiddleRAT)	1	12	0	26	22	0	0	0	39	0	100	0.87	200–270
B035RR0 (Guadalupe_King3)	1	9	0	38	16	0	0	0	36	0	100	0.90	200–270
B038SU0 (FineSoil_PaydirtPri1)	36	41	15	0	0	6[b]	3	3	3[b]	0	100	0.22	250–260
B040RU0 (LastChance_Makar)	0	15	0	29	18	0	0	0	38	0	100	0.85	260–270
B041RU0 (Dells_HiHo)	7	17	0	28	15	0	0	0	33	0	100	0.75	240–260
B043RU0 (FlatRock_Mojo2)	8	17	0	24	19	0	0	0	32	0	100	0.75	260–280
B045RR0 (FlatRock_Mojo2)	1	15	0	22	25	0	0	0	38	0	100	0.85	200–270
B046RU0 (BerryBowl_Empty)	3	12	0	29	20	0	0	0	36	0	100	0.86	240–270
B048RU0 (BerryBowl_MoessBerry)	10	11	16	0	0	0	0	0	63	0	100	0.79	200–280
B049RU0 (RasberryNewton_Filling)	3	12	0	30	19	0	0	0	36	0	100	0.85	240–270
B051RU0 (RealSharksTooth_Enamel1)	1	8	0	22	15	0	0	0	54	0	100	0.91	200–280
B052SU0 (Goal5WorkVolume_Panaluu)	9	12	7	0	0	7[b]	4	2	65	0	100	0.78	250–270
B053SU0 (Goal3Field_Vanilla2)	39	25	11	0	0	6[b]	4	2	20[b]	0	100	0.35	260–270
B054SU0 (MudPie_Coconut2)	37	33	15	0	0	5[b]	4	1	10[b]	0	100	0.30	240–260
B055SU0 (Meringue_MBone)	36	37	16	0	0	6[b]	1	5	5[b]	0	100	0.24	230–240
B056SU0 (BlackForest_BriansChoice)	33	37	14	0	0	9[b]	1	8	8[b]	0	100	0.27	250–260
B060SU0 (MontBlanc_LesHauches)	28	32	30	0	0	5[b]	2	4	5[b]	0	100	0.39	200–280
Eagle-Endurance Intercrater Plains, Meridiani Planum													
B062SU0 (BlackPatch_Munter)	29	29	14	0	0	9[b]	4	5	20[b]	0	100	0.40	250–260
B063SU0 (Whitestreak_Cleo3)	13	19	10	0	0	4[b]	2	2	55[b]	0	100	0.67	250–260
B066RU0 (BounceRock_Glanz2)	0	100	0	0	0	0	0	0	0	0	100	0.00	200–260
B067RR0 (BounceRock_Case)	0	100	0	0	0	0	0	0	0	0	100	0.00	200–260
B067RU0 (BounceRock_Eifel)	0	99	1	0	0	0	0	0	0	0	100	0.01	250–260
B067RU0 (BounceRock_Loreley)	0	100	0	0	0	0	0	0	0	0	100	0.00	250–260
B068RU0 (BounceRock_Fips2)	0	100	0	0	0	0	0	0	0	0	100	0.00	200–250
B069RU0 (BounceRock_Grace)	0	98	2	0	0	0	0	0	0	0	100	0.02	240–260
B069RU0 (BounceRock_Wrigley2)	0	97	3	0	0	0	0	0	0	0	100	0.03	250–260
B070RU0 (BounceRock_Maggie)	0	98	2	0	0	0	0	0	0	0	100	0.02	200–210
B073SU0 (Seas_AegeanCrest)	11	12	5	0	0	8[b]	5	3	65[b]	0	100	0.76	250–270
B078ST1 (DogPark_JeffsChoice)	32	39	16	0	0	7[b]	3	3	6[b]	0	100	0.27	230–270
B080SU0 (DogPark_JackRussell)	17	19	9	0	0	0	0	0	56	0	100	0.64	260–270
B084SU0 (Nullarbor_GreatSandy)	13	16	7	0	0	4[b]	1	3	61[b]	0	100	0.70	250–260
B085RU0 (Baseball_Infield)	2	8	0	35	22	0	0	0	33	0	100	0.91	240–260
B088RR0 (Pilbara_Golf)	0	10	0	33	20	0	0	0	37	0	100	0.90	200–260
B090SD0 (PhotoTIDD_Nougat)	27	31	23	0	0	7[b]	3	4	12[b]	0	100	0.40	200–260
B091RU0 (PhotoTIDD_FredRipple)	15	17	9	0	0	7[b]	3	4	51[b]	0	100	0.66	250–270
B097SU0 (BerryStop_LeahsChoice)	16	19	13	0	0	5[b]	2	4	47[b]	0	100	0.63	230–260
B105RU0 (LionStone_Nala)	0	16	0	32	21	0	0	0	31	0	100	0.84	240–260
B108RR0 (LionStone_NummaNewNormal)	1	14	0	30	22	0	0	0	34	0	100	0.86	250–260
B121RU0 (FigTree_Barberton2)	51	32	6	0	0	0	0	0	0	11	100	0.06	230–270
B123SU0 (HillTop_McDonnell)	33	36	19	0	0	8[b]	2	6	4[b]	0	100	0.28	240–270
B124RU0 (Pyrrho_Sweet)	4	16	0	29	19	0	0	0	31	0	100	0.80	250–270
B126RU0 (Diogenes_MyTier02)	5	14	0	24	19	0	0	0	38	0	100	0.81	230–250
Endurance Crater, Meridiani Planum													
B140RR0 (Tennessee_Vols)	1	14	0	29	18	0	0	0	39	0	100	0.85	200–250
B142RU0 (Kentucky_BlueGrass2)	9	20	0	21	14	0	0	0	36	0	100	0.71	250–260
B143RU0 (Kentucky_Churchill)	5	14	0	26	16	0	0	0	38	0	100	0.80	200–250
B144RR0 (Kentucky_CobbleHill)	1	15	0	28	20	0	0	0	35	0	100	0.84	200–260
B148RR0 (LayerC_Virginia)	2	16	0	28	19	0	0	0	35	0	100	0.82	200–260
B150RR0 (Ontario_London)	1	18	0	27	19	0	0	0	35	0	100	0.81	200–260
B152RR0 (Manitoba_Grindstone)	2	17	0	28	20	0	0	0	34	0	100	0.81	200–260
B154RR0 (Manitoba_Kettlestone)	2	15	0	29	21	0	0	0	32	0	100	0.82	200–270
B163RR0 (Millstone_Drammensfjord)	1	21	0	27	18	0	0	0	33	0	100	0.78	200–260
B165SU0 (Millstone_Dahlia)	38	40	14	0	0	5[b]	1	5	3[b]	0	100	0.20	210–260
B174RU0 (Hoghead_ArnoldZiffel)	5	17	0	24	17	0	0	0	36	0	100	0.77	230–240
B179RR0 (DiamondJenness_Holman3)	2	11	0	29	18	0	0	0	41	0	100	0.88	200–250
B183RR0 (Mackenzie_Campbell2)	1	15	0	31	19	0	0	0	34	0	100	0.84	220–250

Table 3. (continued)

Generic Name / Phase Assignment	Fe2D1 Ol, %	Fe2D2 Px, %	Fe3D1 npOx, %	Fe3D4 Jar, %	Fe3D3 Fe3D3, %	Mt, %	Fe3S1 Mt(3), %	Fe2.5S1 Mt(2.5), %	Fe3S2 Hm, %	Fe0S1 α-(Fe,Ni)^0, %	Sum, %	Fe^{3+}/Fe_T	T, K
B188RR0 (Inuvik_Tuktoyaktuk)	2	14	0	26	18	0	0	0	40	0	100	0.84	200–260
B196RR0 (Bylot_Aktineq3)	2	13	0	30	14	0	0	0	41	0	100	0.85	210–260
B198RU0 (Bylot_Sermilik)	6	12	0	24	20	0	0	0	37	0	100	0.81	240–260
B211RU0 (Escher_AfarMB)	3	13	0	29	21	0	0	0	34	0	100	0.84	210–260
B213RU0 (Escher_Kirchner)	4	16	0	28	19	0	0	0	32	0	100	0.80	210–260
B215RB0 (Escher_Kirchner)	1	15	0	29	21	0	0	0	33	0	100	0.84	210–260
B217RB0 (Escher_EmilNolde)	8	16	0	25	26	0	0	0	25	0	100	0.76	210–260
B219RR0 (Escher_Kirchner)	1	15	0	30	20	0	0	0	35	0	100	0.84	210–270
B222SU0 (BerrySurvey_Cluster3)	16	19	9	0	0	2[b]	0	2	54[b]	0	100	0.64	200–260
B237SB0 (Auk_AukRAT)	38	40	14	0	0	6[b]	2	4	1[b]	0	100	0.20	210–260
B241RU0 (Ellesmere_Barbeau3)	7	17	0	32	17	0	0	0	27	0	100	0.77	210–250
B246SU0 (Rocknest_VoidMod)	40	37	13	0	0	7[b]	2	5	3[b]	0	100	0.21	190–240
B308RR0 (Blackcow_Wharenhui)	5	14	0	28	19	0	0	0	34	0	100	0.81	190–270
Endurance-Erebus Intercrater Plains, Meridiani Planum													
B348RU0 (SpongeBob_Squidward)	0	0	4	0	0	0	0	0	0	96	100	0.04	210–270
B351RB0 (SpongeBob_Squidward)	0	0	6	0	0	0	0	0	0	94	100	0.06	210–270
B367ST1 (Trench_LeftOfPeanut)	32	38	19	0	0	7[b]	2	5	4[b]	0	100	0.27	210–280
B368SU0 (TrenchRipple_RippleCrest2b)	12	13	7	0	0	0	0	0	68	0	100	0.75	250–280
B369SU0 (TrenchRipple_CavairTweaked)	21	32	10	0	0	7[b]	3	4	30[b]	0	100	0.45	260–280
B373SD0 (Trench_Scruffy)	30	47	13	0	0	7[b]	2	5	4[b]	0	100	0.21	250–280
B380RU0 (Russett_BridgeOfNose)	0	11	0	33	22	0	0	0	34	0	100	0.89	250–280
B392RU0 (Normandy_Omaha)	1	6	0	34	25	0	0	0	34	0	100	0.93	210–280
B404RR0 (Yuri_Gagarin)	1	7	0	32	24	0	0	0	37	0	100	0.92	210–270
B415SU0 (MattsRipple_Mobarak)	17	21	11	0	0	2[b]	0	2	48[b]	0	100	0.61	190–270
B419SU0 (Ripple_Norooz)	17	18	11	0	0	0	0	0	53	0	100	0.65	250–290
B420SU0 (Ripple_Mayberooz)	17	17	11	0	0	0	0	0	55	0	100	0.66	250–290
B445SD0 (RecoverySoil_Cure)	18	18	11	0	0	3[b]	1	2	50[b]	0	100	0.63	190–270
B509SD0 (Purgatory_Track2)	22	27	30	0	0	5[b]	2	3	15[b]	0	100	0.49	190–270
B548RR0 (IceCream_Onescoop)	3	10	0	32	19	0	0	0	36	0	100	0.87	200–270
B551RU0 (Cobbles_Arkansas)	6	15	52	19	0	0	0	0	8	0	100	0.79	200–270
B557RB0 (FruitBasket_LemonRind)	6	13	0	33	18	0	0	0	30	0	100	0.81	210–270

[a]Uncertainty in subspectral area is ±2% absolute unless otherwise stated.
[b]Uncertainty in subspectral area is ±3% absolute.
[c]Because Mt = Mt(3) + Mt(2.5), Sum = Ol + Px + npOx + Jar + Fe3D3 + Mt + Hm + α-(Fe,Ni)^0.
[d]Fe^{3+}/Fe_T = (npOx + Jar + Fe3D3 + Mt(3) + 0.5(Mt(2.5)) + Hm)/Sum. Uncertainty in Fe^{3+}/Fe_T is ±0.03.

finally, phase assignments made by MER instruments as an aggregate must be mutually consistent. For example, olivine and pyroxene are identified in rocks and soils at Gusev crater by both MB and MiniTES instruments.

3.2. Rock and Soil Classification

[18] Gusev crater rocks are organized into six named classes on the basis of APXS chemistry [*Gellert et al.*, 2006; *Squyres et al.*, 2006a; *Ming et al.*, 2006]. On the basis of large differences in Fe mineralogical composition, we formed a number of subclasses [*Morris et al.*, 2006]. In addition, we organized Gusev crater soils into two named classes (Laguna Class and Paso Robles Class). We classified Meridiani Planum rocks and soils using as much as possible the classification scheme developed for Gusev crater (Table 4). There are two rock classes: (1) Burns Outcrop Class and (2) Other Rocks Class. The former is the S-rich outcrop and the latter includes all other rocks (Bounce Rock, Heat Shield Rock, and a collection of cobbles). As of Opportunity sol 557, there are no rocks common to Gusev crater and Meridiani Planum on the basis of elemental composition.

[19] Soils at Meridiani Planum are classified using the Laguna Class from Gusev crater and Berry Class (Table 4). Laguna Class is basaltic soil with Ol, Px, npOx and minor Hm and Mt as the Fe-bearing phases. As discussed later, Berry Class has higher Fe concentrations and Hm is a major Fe-bearing phase resulting from Hm-rich spherules and their fragments.

3.3. Representative Meridiani Planum Mössbauer Spectra

[20] In Figure 1 we show representative MB spectra for Meridian Planum along with the component subspectra obtained from the fitting procedures. We were able to describe all Meridiani Planum spectra with five doublet and four sextet subspectra: two doublets from octahedrally coordinated Fe^{2+} (oct-Fe^{2+}) (Fe2D1 and Fe2D2), three doublets from oct-Fe^{3+} (Fe3D1, Fe3D3, and Fe3D4), one sextet from tetrahedrally coordinated Fe^{3+} (tet-Fe^{3+}) (Fe3S1), one sextet from coupled oct-Fe^{2+} and Fe^{3+} (Fe2.5S1), one sextet from oct-Fe^{3+} (Fe3S2), and one sextet from Fe metal (Fe0S1). This description assumes a one-doublet fit (using Fe2D2) for spectra from Bounce Rock. A superior fit is obtained with a two-doublet model (both oct-Fe^{2+}), and the results are given as a footnote in Table 1. The fitting of individual Meridiani Planum spectra required

Table 4. Classification of Meridiani Planum Rocks and Soils Through Sol 557

Class	Rocks/Soils
	Meridiani Planum Rocks[a]
Burns Outcrop Class	B016RU0 (StoneMountain_RobertE), B027RU0 (StoneTablet_Shalt), B029RU0 (McKittrick_MiddleRAT), B030RU0 (Guadalupe_RATLower), **B032RR0 (McKittrick_MiddleRAT)**, **B035RR0 (Guadalupe_King3)**, B039RU0 (LastChance_Makar), B041RU0 (Dells_HiHo), B043RU0 (FlatRock_Mojo2), **B045RR0 (FlatRock_Mojo2)**, B046RU0 (BerryBowl_Empty), B049RU0 (RasberryNewton_Filling), B051RU0 (RealSharksTooth_Enamel1), B085RU0 (Baseball_Infield), **B088RR0 (Pilbara_Golf)**, B105RU0 (LionStone_Nala), **B108RR0 (LionStone_NummaNewNormal)**, B124RU0 (Pyrro_Sweet), B126RU0 (Diogenes_MyTier02), **B140RR0 (Tennessee_Vols)**, B142RU0 (Kentucky_BlueGrass2), B143RU0 (Kentucky_Churchill), **B144RR0 (Kentucky_CobbleHill)**, **B148RR0 (LayerC_Virginia)**, **B150RR0 (Ontario_London)**, **B152RR0 (Manitoba_Grindstone)**, **B154RR0 (Manitoba_Kettlestone)**, **B163RR0 (Millstone_Drammens)**, B174RU0 (Hoghead_ArnoldZiffel), **B179RR0 (DiamondJennes_Holman3)**, **B183RR0 (Mackenzie_Campbell2)**, **B188RR0 (Inuvik_Tuktoyaktuk)**, **B196RR0 (Bylot_Aktineq3)**, B198RU0 (Bylot_Sermilik), B211RU0 (Esher_Afar), B213RU0 (Esher_Kirchner), B215RB0 (Esher_Kirchner), B217RB0 (Esher_EmilNolde), **B219RR0 (Esher_Kirchner)**, B241RU0 (Ellesmere_Barbeua3), B261RU0 (Wopmay_Otter), **B308RR0 (Blackcow_Wharenhui)**, B392RU0 (Normandy_Omaha), **B404RR0 (Yuri_Gagarin)**, **B548RR0 (IceCream_Onescoop)**, B557RB0 (FruitBasket_LemonRind).
Other Rocks Class	B066RU0 (BounceRock_Glanz2), **B067RR0 (BounceRock_Case)**, B067RU0 (BounceRock_Eifel), B067RU0 (BounceRock_Loreley), B068RU0 (BounceRock_Fips2), B069RU0 (BounceRock_Grace), B069RU0 (BounceRock_Wrigley2), B070RU0 (BounceRock_Maggie), B121RU0 (FigTree_Barberton2), B348RU0 (SpongeBob_Squidward), B351RB0 (SpongeBob_Squidward), B380RU0 (Potato_Russett), B551RU0 (Cobbles_Arkansas)
	Meridiani Planum Soils
Laguna Class Soil, Panda Subclass	B011SU0 (Merlot_Tarmac), B038SU0 (FineSoil_Paydirt), B165SU0 (Millstone_Dahlia), B237SB0 (Auk_AukRAT), B246SU0 (Rocknest_VoidMod), B373SD0 (Trench_Scruffy)
Laguna Class Soil, Liberty Subclass	B055SU0 (Meringue_MBone), B056SU0 (BlackForest_BriansChoice), B078ST1 (DogPark_JeffsChoice), B123SU0 (HillTop_McDonnell), B367ST1 (TrenchSite_LeftOfPeanut)
Laguna Class Soil, Gobi Subclass	B025ST2 (BigDig_HemaTrench1), B026ST1 (BigDig_HemaTrenchWall2), B060SU0 (MontBlanc_LesHauches)
Berry Class Soil, Nougat Subclass	B017SU0 (BerryFlats_Freckles), B023SU0 (HematiteSlope_Hema2), B053SU0 (Goal3Field_Vanilla2), B054SU0 (MudPie_Coconut2), B062SU0 (BlackPatch_Munter), B090SD0 (PhotoTIDD_Nougat), B369SU0 (TrenchRipple_CavairTweaked), B509SD0 (Purgatory_Track2)
Berry Class Soil, MoessBerry Subclass	B048RU0 (BerryBowl_MoessBerry), B052SU0 (Goal5WorkVolume_Panaluu), B063SU0 (Whitestreak_Cleo3), B073SU0 (Seas_AegeanCrest), B080SU0 (DogPark_JackRussell), B084SU0 (Nullarbor_GreatSandy), B091RU0 (PhotoTIDD_FredRipple), B097SU0 (BerryStop_LeahsChoice), B222SU0 (BerrySurvey_Cluster3), B368SU0 (TrenchRipple_RippleCrest2b), B415SU0 (MattsChoice_Mobarak), B419SU0 (Ripple_Norooz), B420SU0 (Ripple_Mayberooz), B445SU0 (RecoverySoil_Cure)

[a]Targets in bold font are analyses of rock surfaces exposed by grinding with the RAT.

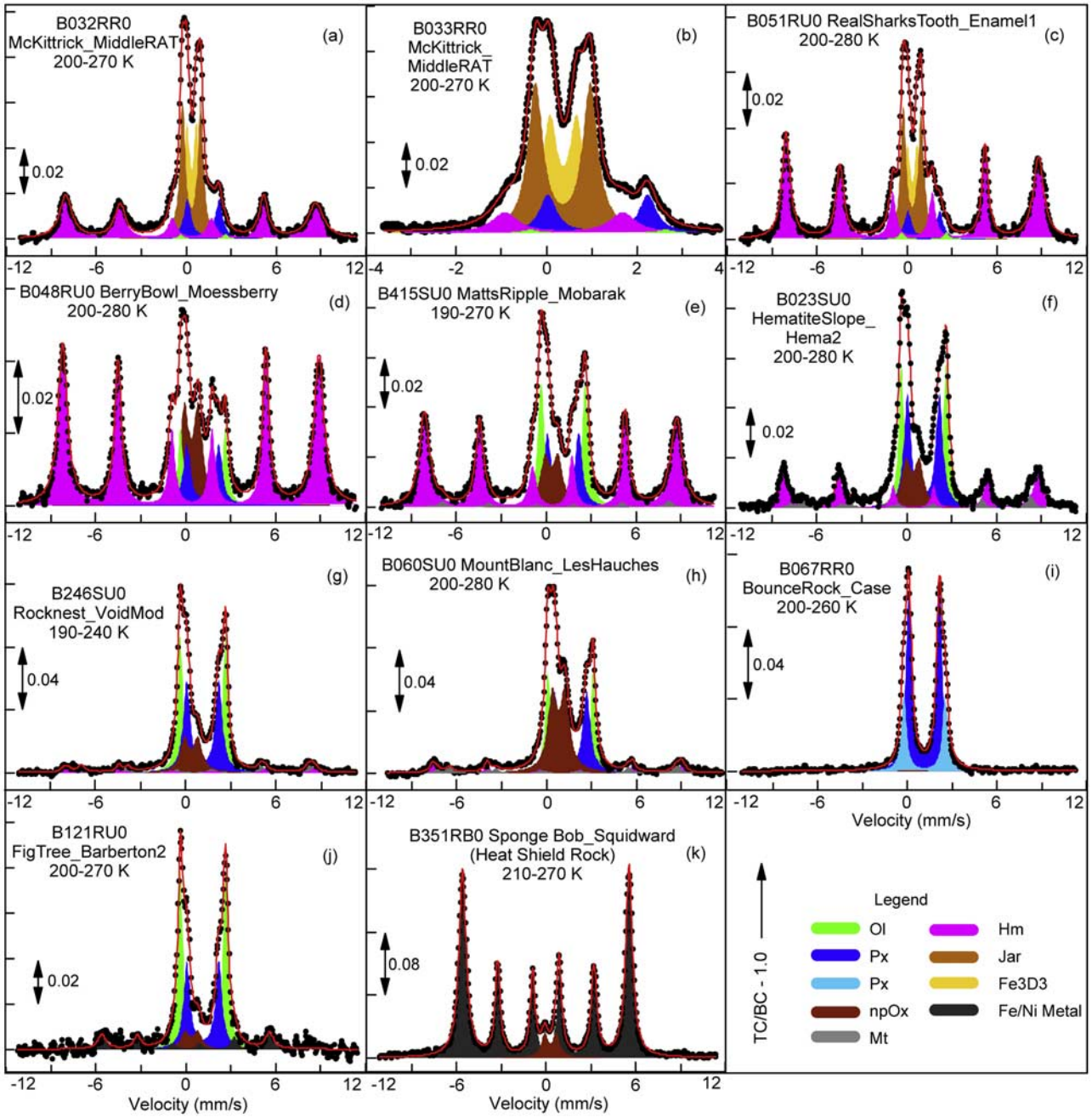

Figure 1. Representative Mössbauer spectra from Meridiani Planum. Spectra are the sum over all temperature windows within the indicated temperature ranges. The computed fit and component subspectra (Lorentzian line shapes) from least squares analyses are shown by the solid red line and the solid shapes, respectively. (a) Full and (b) reduced velocity MB spectra for interior Burns outcrop exposed by RAT grinding show that hematite, jarosite, and Fe3D3 (unidentified Fe^{3+} phase) are the major Fe-bearing phases. (c) MB spectrum for a rind or crust of outcrop material that has an increased contribution of hematite relative to jarosite plus Fe3D3. (d and e) MB spectra of two MoessBerry Subclass soils that have high concentrations of hematite. The spectrum in Figure 1e is typical for hematite lag deposits at ripple crests. (f) The MB spectrum of a Nougat Subclass soil is transitional between MoessBerry Subclass soil and Laguna Class soil. Example MB spectra of the (g) Panda and (h) Gobi Subclasses of Laguna Class soil are basaltic in nature and have olivine, pyroxene, and npOx as their major Fe-bearing phases. MontBlanc_LesHauches is considered to be enriched in Martian dust. MB spectra in Figures 1i–1k are for three single-occurrence rocks. (i) BounceRock is monomineralic pyroxene with respect to Fe-bearing phases. (j) Barberton contains metallic iron, and (k) Heat Shield Rock is nearly monomineralic kamacite (Fe-Ni metal alloy with ~5% Ni). TC, total counts; BC, baseline counts.

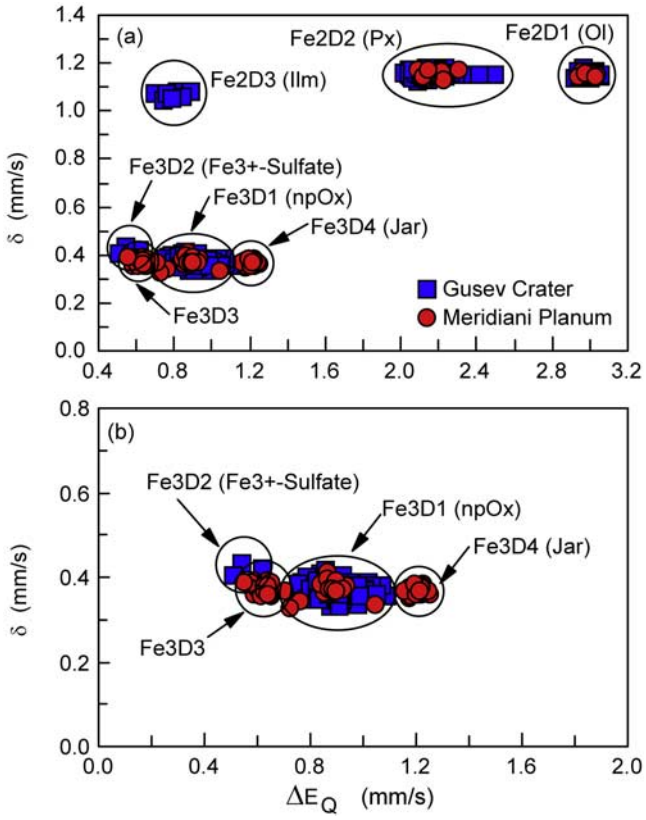

Figure 2. Phase identification plots (isomer shift versus quadrupole splitting) for doublet MB subspectra for targets from Gusev crater (solid blue squares) and Meridiani Planum (solid red circles). The region near the origin in Figure 2a is expanded in Figure 2b. Parameters were calculated from spectra summed over all temperature windows within the temperature ranges given in Table 1. Data points cluster according to Fe oxidation state and mineralogical composition. At Meridiani Planum, two Fe^{2+}-bearing phases (olivine and pyroxene) and three Fe^{3+}-bearing phases (npOx, jarosite, and Fe3D3) are identified on the plots.

between two and seven subspectra. Doublets Fe3D3 and Fe3D4 and sextet Fe0S1 were not observed at Gusev crater.

3.4. Mineralogical Assignment of Doublet Subspectra

[21] We show a plot (Figure 2) of δ versus ΔE_Q for samples from Gusev Crater [*Morris et al.*, 2006] and Meridiani Planum. All data were calculated from MB spectra that are a sum of spectra over the indicated temperature interval (Table 1 in this study and of *Morris et al.* [2006]). The temperature dependences of δ and ΔE_Q are shown in Figure 3. The data for Fe2D1, Fe2D2, and Fe3D1 for Gusev Crater and Meridiani Planum (Figures 3a–3f) are not distinguishable, so that the same three Fe-bearing phases are present at both locations. As discussed by *Morris et al.* [2006], the three doublets are assigned to Fe^{2+} in olivine (Ol), Fe^{2+} in pyroxene (Px), and Fe^{3+} in nanophase ferric oxide (npOx), respectively. At Meridiani Planum, they are the dominant Fe-bearing phases in soil, BounceRock, and the small rock Barberton. BounceRock is virtually monomineralic Px with respect to Fe-bearing phases.

[22] Two doublets (Fe3D3 and Fe3D4) were not detected at Gusev crater, and they are both associated with the S-rich outcrop rock (the Burns Formation) at Meridiani Planum. For summed spectra, the average values of δ and ΔE_Q are 0.37 ± 0.02 mm/s and 0.62 ± 0.03 mm/s for Fe3D3 and 0.37 ± 0.02 mm/s and 1.20±0.02 mm/s for Fe3D4. The parameters are at most weakly dependent on temperature (Figures 3g–3j) and are the same within error as the values obtained at room temperature (295 K) by extrapolation (Table 5). The value of ΔE_Q for Fe3D4 is unusually high for oct-Fe^{3+}, and it was assigned to the mineral jarosite by *Klingelhöfer et al.* [2004]. We use the generalized formula $(K, Na, H_3O)(Fe, Al)_3(SO_4)_2(OH, Cl)_6$ where Fe ≫ Al and OH ≫ Cl for "jarosite" at Meridiani Planum recognizing that stoichiometric jarosite is $KFe_3(SO_4)_2(OH)_6$. For purposes of comparison, we compiled MB data for a number of terrestrial and synthetic jarosite samples from the literature (Table 6). We have also measured the temperature dependence of δ and ΔE_Q for several jarosites using the flight spare MIMOS II instrument where sample and instrument were in a chamber whose temperature could be controlled (Table 6). We found no temperature dependence for either parameter for the samples or the inferred Martian jarosite.

[23] In his study of synthetic, Al-free jarosites, *Leclerc* [1980] found that ΔE_Q increased with the degree of Fe deficiency in the jarosite, which also increases from H_3O to Na to K as the monovalent cation. The data in Table 6 also indicate that Al^{3+} for Fe^{3+} substitution results in elevated values of ΔE_Q. On the basis of the data in Table 6 and constraints imposed by the concentration of Na and K in the outcrop [*Rieder et al.*, 2004; R. Gellert, manuscript in preparation, 2006], Meridiani Planum jarosite has Na > K > H_3O with possible Al^{3+} for Fe^{3+} substitution. We included chloride in our generalized formula because the anion is available according to APXS data (0.5–2.0 % [*Rieder et al.*, 2004; R. Gellert, manuscript in preparation, 2006]). Additional work for Al- and Cl-bearing jarosites is needed to further constrain the elemental composition of jarosite in the Burns formation. Jarosite formation from alteration of basaltic materials is known on the Earth [e.g., *Morris et al.*, 1996, 2000; *Bishop et al.*, 1998], but the spatial extents of the terrestrial occurrences are small compared to the sulfate-rich Burns formation. The presence of jarosite and other sulfate minerals on Mars was advocated in a series of papers by the late Roger Burns [*Burns*, 1986, 1987, 1988, 1993; *Burns and Fisher*, 1990].

[24] The correspondence in values of δ and ΔE_Q for Fe3D4 and synthetic and natural jarosite samples permits the assignment of Fe3D4 to jarosite. But is this assignment unique? Are there other, geologically reasonable, Fe-bearing phases that also have the same MB parameters? We have examined the databases referenced above and have not found reasonable alternatives for jarosite. Either an alternative phase is characterized by MB parameters that are not appropriate for Fe3D4 or its MB spectrum has more than one doublet.

[25] We have insufficient constraints to make an assignment for the Fe3D3 doublet. The relative proportions of the three major Fe-bearing phases in the outcrop are nearly

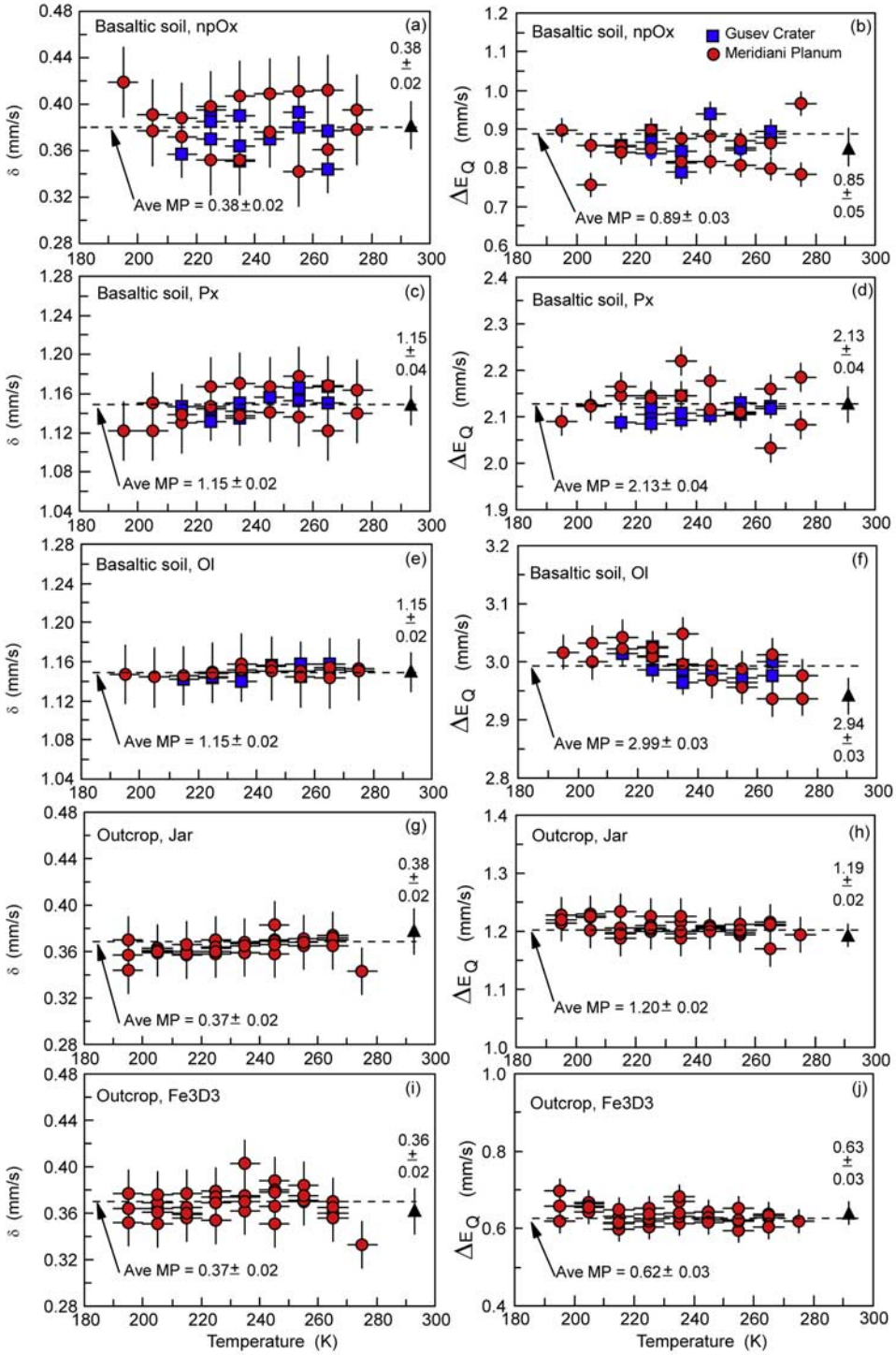

Figure 3. Isomer shift and quadrupole splitting as a function of temperature for (a and b) npOx, (c and d) pyroxene, (e and f) olivine, (g and h) jarosite, and (i and j) Fe3D3. Horizontal dashed lines are average ± 1σ for MB spectra (Meridiani Planum targets) summed over all temperature windows. The solid triangles are the values extrapolated to 295 K from the straight-line least squares fit of the data shown.

constant with A_{Jar} = 29 ± 3 %, A_{Fe3D3} = 19 ± 3 %, and A_{Hm} = 35 ± 4 % as average values, implying jarosite, Fe3D3, and hematite are always formed in approximately fixed proportions. It is possible that Fe3D3 is a form of npOx that is different from the npOx found in typical basaltic (Laguna Class) soils or perhaps a phyllosilicate phase [*Klingelhöfer et al.*, 2004]. Possible npOx end-member compositions for Fe3D3 include the superparamagnetic forms of hematite

Table 5. Temperature Dependence of δ and ΔE_Q for Doublet Subspectra at Meridiani Planum, Extrapolated Values of δ and ΔE_Q at 295 K, and Average Values of δ and ΔE_Q for Spectra Summed Over All Temperature Windows

Generic Name	Assignment	δ Gradient ($\times 10^{-4}$ mm/s/K)	δ at 295 K, mm/s	Ave δ for Sum, mm/s	ΔE_Q Gradient ($\times 10^{-4}$ mm/s/K)	ΔE_Q at 295K, mm/s	Ave ΔE_Q for Sum, mm/s
Fe3D1	Basaltic soil, npOx	-0.84 ± 2.4[a]	0.38 ± 0.02	0.38 ± 0.02	0.57 ± 5.1	0.85 ± 0.05	0.89 ± 0.03
Fe3D3	Outcrop, unassigned	0.42 ± 0.08	0.36 ± 0.02	0.37 ± 0.02	-0.17 ± 0.13	0.63 ± 0.03	0.62 ± 0.03
Fe3D4	Outcrop, Jar	1.9 ± 0.6	0.38 ± 0.02	0.37 ± 0.02	-2.5 ± 1.3	1.19 ± 0.02	1.20 ± 0.02
Fe2D1	Basaltic soil, Ol	0.69 ± 0.41	1.15 ± 0.02	1.15 ± 0.02	-9.4 ± 4.8	2.94 ± 0.03	2.99 ± 0.03
Fe2D2	Basaltic soil, Px	1.6 ± 4.1	1.15 ± 0.04	1.15 ± 0.02	0.093 ± 1.8	2.13 ± 0.04	2.13 ± 0.02
Fe2D2	BounceRock, Px (1D)[b]	3.4 ± 1.2	1.17 ± 0.01	1.15 ± 0.02	-10.0 ± 5.0	2.15 ± 0.03	2.21 ± 0.02
Fe2D2	BounceRock, Px (2D)[b]	4.0 ± 1.2	1.17 ± 0.01	1.14 ± 0.02	0.26 ± 0.82	2.05 ± 0.05	2.04 ± 0.03
Fe2D2	BounceRock, Px (2D)[b]	3.2 ± 1.7	1.19 ± 0.02	1.17 ± 0.02	-13 ± 20	2.64 ± 0.13	2.73 ± 0.04

[a]Uncertainty is 1σ.
[b]1D, one-doublet model; 2D, two-doublet model.

and goethite, ferrihydrite, akaganeite, and schwertmannite [*Morris et al.*, 2006]. Both jarosite and npOx occur together in samples from the Rio Tinto (Spain) [*Fernandez-Remolar et al.*, 2005], White Island (New Zealand) [*Johnson*, 1977], and Dalarna (Sweden) [*Herbert*, 1997], where the npOx is superparamagnetic goethite or schwertmannite, superparamagnetic goethite or akaganeite, and superparamagnetic goethite, respectively. Their reported values ΔE_Q (for one-doublet fits) are in the range 0.5–0.7 mm/s, which is comparable to the range observed for Fe3D3 (Table 1). The nature of the coexisting phase seems to depend on local conditions. For example, akaganeite is stabilized by the high chloride environment on White Island volcano [*Johnson*, 1977].

3.5. Mineralogical Assignment of Sextet Subspectra

[26] We identified four sextet subspectra in Meridiani Planum MB spectra: Fe3S1 and Fe2.5S1 assigned to tet-

Table 6. Mössbauer Parameters for S-Rich Outcrop at Meridiani Planum, Terrestrial Jarosite-Bearing Samples, and Synthetic Jarosites at Temperatures Between 215 and 295 K

Sample	T, K	δ,[a] mm/s	ΔE_Q, mm/s	Comments (Reference)[b]
Burns Formation, Mars	295	0.37 ± 0.02[c]	1.19 ± 0.02[c]	Sulfate outcrop rock (1)
Burns Formation, Mars	245	0.37 ± 0.02	1.21 ± 0.02[c]	Sulfate outcrop rock (1)
Burns Formation, Mars	215	0.36 ± 0.02	1.21 ± 0.02[c]	Sulfate outcrop rock (1)
HWMK24, <1 mm	295	0.38 ± 0.01	1.19 ± 0.01	Natural, basaltic precursor (2)
HWMK24, <1 mm	295	0.38 ± 0.02	1.14 ± 0.02	Natural, basaltic precursor (1)[d]
HWMK24, <1 mm	245	0.38 ± 0.02	1.15 ± 0.02	Natural, basaltic precursor (1)[d]
HWMK24, <1 mm	215	0.38 ± 0.02	1.15 ± 0.02	Natural, basaltic precursor (1)[d]
HWMK24, <5 μm	295	0.36 ± 0.01	1.15 ± 0.01	Natural, basaltic precursor (2)
WI30[e]	295	0.376 ± 0.012	1.244 ± 0.012	Natural, andesitic precursor (3)
WI32[e]	295	0.375 ± 0.005	1.240 ± 0.005	Natural, andesitic precursor (3)
WI300R[e]	295	0.393 ± 0.005	1.238 ± 0.005	Natural, andesitic precursor (3)
LNVJAR1	295	0.36 ± 0.01	1.19 ± 0.01	Natural, natrojarosite (2)
LNVJAR1	295	0.38 ± 0.02	1.20 ± 0.02	Natural, natrojarosite (1)[d]
GCJAR1	295	0.33 ± 0.01	1.20 ± 0.01	Natural, K-rich jarosite (2)
GCJAR1	295	0.38 ± 0.02	1.18 ± 0.02	Natural, K-rich jarosite (1)[d]
GCJAR1	245	0.38 ± 0.02	1.18 ± 0.02	Natural, K-rich jarosite (1)[d]
GCJAR1	215	0.38 ± 0.02	1.19 ± 0.02	Natural, K-rich jarosite (1)[d]
TT#12	295	0.33 ± 0.01	1.22 ± 0.01	Natural (2)
TT#35	295	0.33 ± 0.01	1.20 ± 0.01	Natural (2)
KF01-09	295	0.38 ± 0.02	1.01 ± 0.02	Natural, hydronium jarosite (4)
KF01-12	295	0.37 ± 0.02	1.13 ± 0.02	Natural, natrojarosite (4)
KF03-112	295	0.37 ± 0.02	1.19 ± 0.02	Natural, natrojarosite (4)
J14	295	0.39	1.10	Natural (5)
1092	295	0.38	1.12	Natural, (K,Na)-jarosite (5)
$K(Fe_{2.5}Al_{0.5})(SO_4)_2(OH)_6$	295	0.40 ± 0.05	1.25 ± 0.05	Natural, K-jarosite (6)
$H_3OFe_3(SO_4)_2(OH)_6$	295	0.40 ± 0.05	1.00 ± 0.05	Synthetic, H_3O-jarosite (6)
$NaFe_3(SO_4)_2(OH)_6$	295	0.40 ± 0.05	1.05 ± 0.05	Synthetic, Na-jarosite (6)
$KFe_3(SO_4)_2(OH)_6$	295	0.40 ± 0.05	1.15 ± 0.05	Synthetic, K-jarosite (6)
$H_3OFe_{2.94}(SO_4)_2(OH)_6$	295	0.388 ± 0.005	1.01 ± 0.01	Synthetic, H_3O-jarosite (7)
$(Na_{0.82},H_3O_{0.18})Fe_{2.80}(SO_4)_2(OH)_6$	295	0.384 ± 0.005	1.06 ± 0.01	Synthetic, Na-jarosite (7)
$(K_{0.86},H_3O_{0.14})Fe_{2.49}(SO_4)_2(OH)_6$	295	0.384 ± 0.005	1.13 ± 0.01	Synthetic, K-jarosite (7)

[a]δ is relative to metallic Fe foil at the measurement temperature.
[b]References: 1, this study; 2, *Morris et al.* [1996]; 3, *Johnson* [1977]; 4, *Fernandez-Remolar et al.* [2005]; 5, *Herbert* [1997]; 6, *Hrynkiewicz et al.* [1965]; 7, *Leclerc* [1980].
[c]From Figure 3.
[d]Measured with MIMOS II Flight Model 1 instrument.
[e]Composition of jarosite in WI30 is $(K_{0.56}Na_{0.39}H_3O_{0.05})(Fe_{0.84}Al_{0.16})_3(SO_4)_2(OH)_6$ and is presumably representative for WI32, and WI300R.

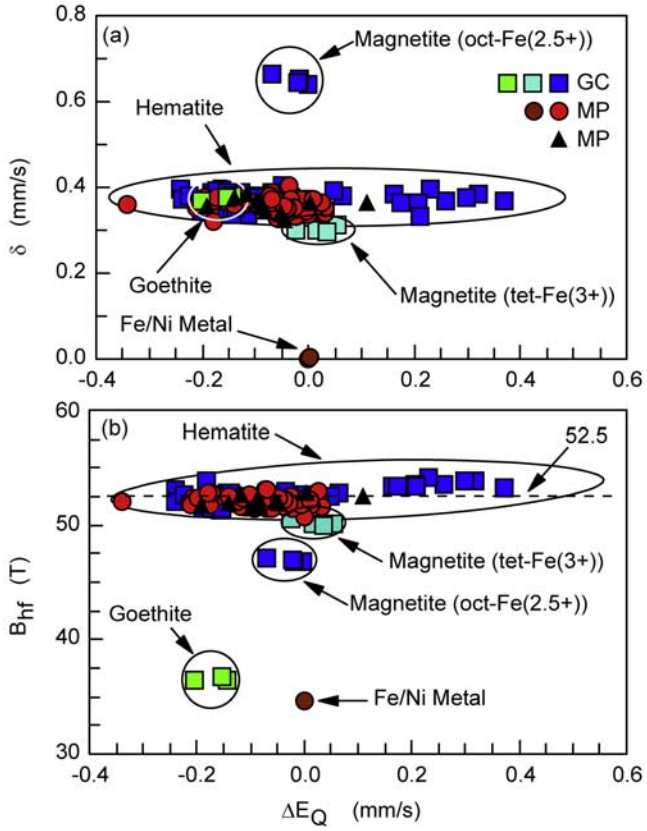

Figure 4. Phase identification plots ((a) isomer shift and (b) hyperfine field strength versus quadrupole splitting) for sextet subspectra for targets from Gusev crater (solid blue, aqua, and green squares) and Meridiani Planum (solid red and brown circles). With one exception, the parameters were calculated from spectra summed over all temperature windows within the temperature ranges given in Table 1. The filled triangles are from the individual temperature windows of sample RealSharksTooth_Enamel1. The distribution of values for hematite results because its Morin transition (~260 K in bulk, well-crystalline, chemically pure hematite) occurs within the Martian diurnal temperature cycle. At Meridiani Planum, three sextet phases were identified: hematite, magnetite, and metallic Fe (kamacite).

Fe^{3+} and oct-(Fe^{2+},Fe^{3+}) in magnetite (Fe_3O_4) at Gusev crater [*Morris et al.*, 2006]; Fe3S2 assigned to oct-Fe^{3+} in hematite (α-Fe_2O_3) at Gusev crater; and Fe0S1, a sextet subspectrum not observed at Gusev crater. Figures 4a and 4b are plots of δ versus ΔE_Q and B_{hf} versus ΔE_Q, respectively, (sextet identification diagrams) for all sextets observed at Gusev crater and Meridiani Planum. Magnetite, hematite, and goethite are readily identified. We will first discuss the Fe3S2 (hematite) sextet.

[27] The data points for hematite do not cluster (Figure 4) because the oxide can undergo a magnetic transition (the Morin transition) at temperatures realized by the Martian diurnal cycle (extreme values of ~180–300 K as measured by the temperature sensor on the MB contact plate). For chemically pure, well-crystalline, and bulk hematite, the Morin transition temperature (T_M) occurs near 260 K, and its manifestation in MB data is most evident by a reversal in the sign of ΔE_Q ($\Delta E_Q < 0.0$ mm/s for $T > T_M$) [e.g., *Greenwood and Gibb*, 1971]. Both substitutional impurities (e.g., Al^{3+}) and the poor crystallinity that accompanies small particle diameters lower T_M and broaden the temperature over which it occurs [e.g., *Murad and Johnson*, 1987; *De Grave and Vandenberghe*, 1990; *Dang et al.*, 1998]. Some impurity ion substitution and/or reduced crystallinity likely accounts for the preponderance of Hm subspectra with $\Delta E_Q < 0.0$ mm/s.

[28] The parameters plotted in Figure 4 were derived from spectra summed over the temperature intervals given in Table 2. This was done to improve counting statistics, but the procedure has the negative consequence of broadening the hematite lines and artificially enlarging the temperature interval over which the Morin transition occurs (for a one-sextet fit for hematite). To demonstrate that the variation in δ and B_{hf} as a function of ΔE_Q for hematite is in fact a result of one doublet fits of two overlapping hematite sextets whose relative intensities vary because of the Morin transition and is not a result of two different Fe-bearing phases, we performed least squares fitting procedures for MB spectra from different temperature windows of the same target. We did these calculations for two outcrop targets (McKittrick_MiddleRAT and Guadalupe_King3), an outcrop rind (RealSharksTooth_Enamel1), a hematite-rich soil (MattsChoice_Mobarak), and unbroken spherules (Berry-Bowl_MoessBerry). In order to have adequate counting statistics, we summed spectra for the lowest (e.g., 200–220 K) and highest (e.g., 250 – 280 K) temperature windows. The derived MB parameters are plotted in Figure 4 as black triangles, and the individual spectra and computed fits are shown in Figure 5. These results show that the variation in δ and B_{hf} as a function of ΔE_Q for spectra of hematite (Figure 4) that are the sum over all temperature windows is a consequence of the hematite Morin transition and different average temperatures over which each sum spectrum was obtained. Another consequence is that the $\Delta E_Q \sim 0.0$ mm/s for some of the spectra should not be construed as evidence for maghemite (γ-Fe_2O_3) which has $\delta \sim 0.32$ mm/s, $\Delta E_Q \sim 0.0$ mm/s, and $B_{hf} \sim 50.0$ T for a one sextet fit at room temperature [e.g., *Morris et al.*, 1985].

[29] We have identified magnetite at Meridiani Planum (mostly in Laguna Class soil), but there are no data points for magnetite from Meridiani Planum in Figure 4. This is because the combination of low magnetite concentration (<9% Fe from Mt) and insufficient counting statistics required constraining magnetite peak parameters (δ, ΔE_Q, and B_{hf}) during fitting procedures to the values we found at Gusev crater [*Morris et al.*, 2006].

[30] Sextet Fe0S1 was detected only at Meridiani Planum in rocks Heat Shield and Barberton (Figure 1). Because the minor npOx component (~5% Fe from npOx) for Heat Shield rock can be a surface contamination of dust or possibly surface oxidation, the sextet probably represents the only Fe-bearing phase in the near surface regions of the rock. The maximum value of the ratio of total counts to baseline counts minus 1.0 (TC/BC – 1.0) for the MB spectrum of Heat Shield rock (~0.24 for SpongeBob_Squidward) is at least twice that for any other sample (Figure 1) and implies a high Fe concentration. The

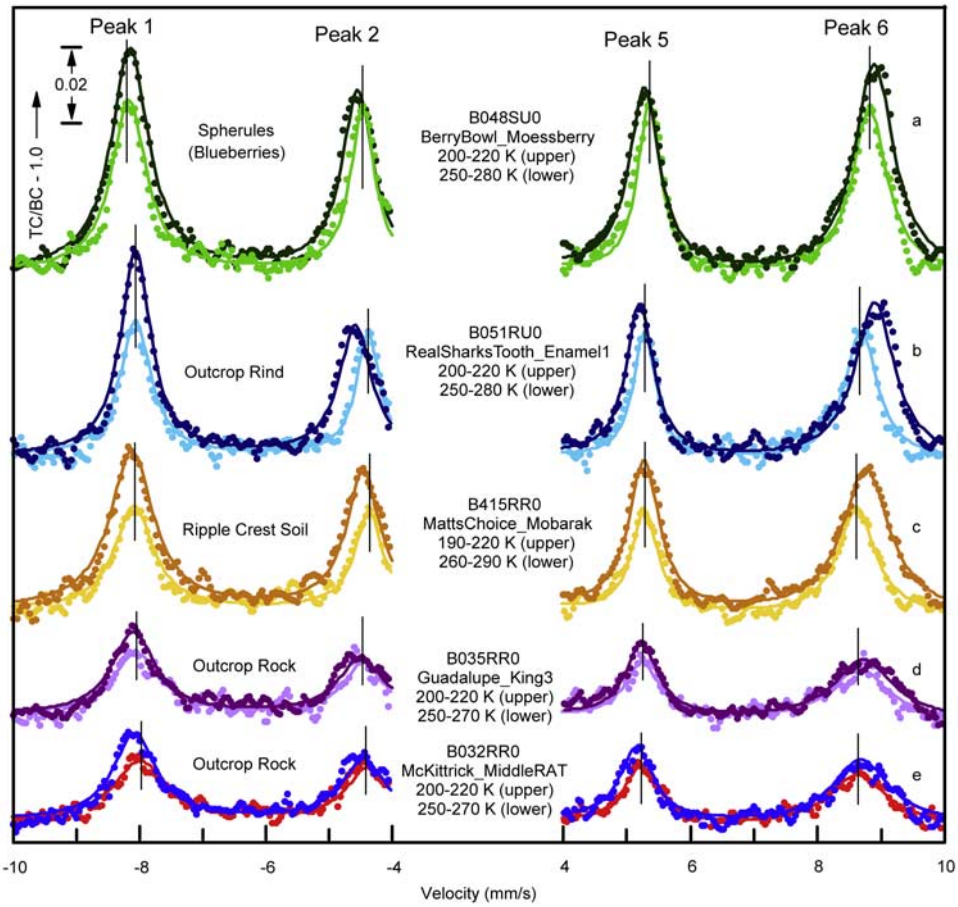

Figure 5. MB spectra showing velocity region with sextet peaks 1, 2, 5, and 6 for BerryBowl_MoessBerry, RealSharksTooth_Enamel1, MattsChoice_Mobarak, Guadalupe_King3, and McKittrick_MiddleRAT. For each target, one spectrum is a sum of spectra over the lowest two or three temperature windows, and the other is a sum over the highest two or three temperature windows. The shift in line positions, particularly for peaks 2 and 6, results from the hematite Morin transition. The solid vertical lines mark the peak centers for the high-temperature spectra.

MB parameters (δ = 0.00 ± 0.02 mm/s, ΔE_Q = 0.00 ± 0.02 mm/s, and B_{hf} = 34.6 ± 0.05 T) identify Fe0S1 as an alloy of α-Fe^0 (metallic iron). The value of B_{hf} is consistent with kamacite, which is an α-$(Fe,Ni)^0$ alloy with 4–7.5% Ni that is commonly found in iron meteorites.

3.6. Summary

[31] Through sol 557 at Meridiani Planum, the Mössbauer spectrometer on the Opportunity rover has detected 8 Fe-bearing phases: two Fe^{2+} silicates (olivine and pyroxene), a mixed Fe^{2+} and Fe^{3+} oxide (magnetite), a Fe^{3+} oxide (hematite), three Fe^{3+} phases (jarosite, npOx, and unassigned Fe3D3), and a metallic Fe alloy (kamacite). Olivine, pyroxene, magnetite, hematite, and npOx are also detected at Gusev Crater [*Morris et al.*, 2006]. Ilmenite, goethite, and Fe3D2 ferric sulfate are detected at Gusev crater and not at Meridiani Planum. Kamacite, jarosite, and unassigned Fe3D3 are detected at Meridiani Planum but not at Gusev crater. The behavior of hematite is complex at both locations because the oxide undergoes a magnetic transition (Morin transition at ~260 K) within the diurnal temperature range on Mars. Jarosite and goethite are the only unequivocal H_2O/OH-bearing phases, and both yield ~10% H_2O upon dehydroxylation. As alteration products, npOx and Fe3D3 also likely contain H_2O/OH, but the evidence is inferential.

4. Mössbauer and APXS Sampling Depths

[32] To compare mineralogical data obtained from the MER MB instrument and elemental data from the MER APXS instrument, the optimal situation is to have exactly the same material analyzed by both instruments. This situation is not as straightforward as it might seem, because the two instruments have different fields of view and because their sampling depths are different. For the MB instrument, the field of view is ~1.5 cm, and the sampling depth in basaltic materials for incident and emitted 14.4 keV emitted radiation is ~0.2 to 3 mm [*Morris et al.*, 2000; *Klingelhöfer et al.*, 2003]. Emitted radiation at both 6.4 and 14.4 keV can be used for the MB experiment, but we consider only spectra for the 14.4 keV radiation in this study. For the APXS instrument, the field of view is ~3.8 cm and the sampling depth is ~1 to 20 μm [*Rieder et al.*, 2003; *Gellert et al.*, 2006]. Assuming that the target being

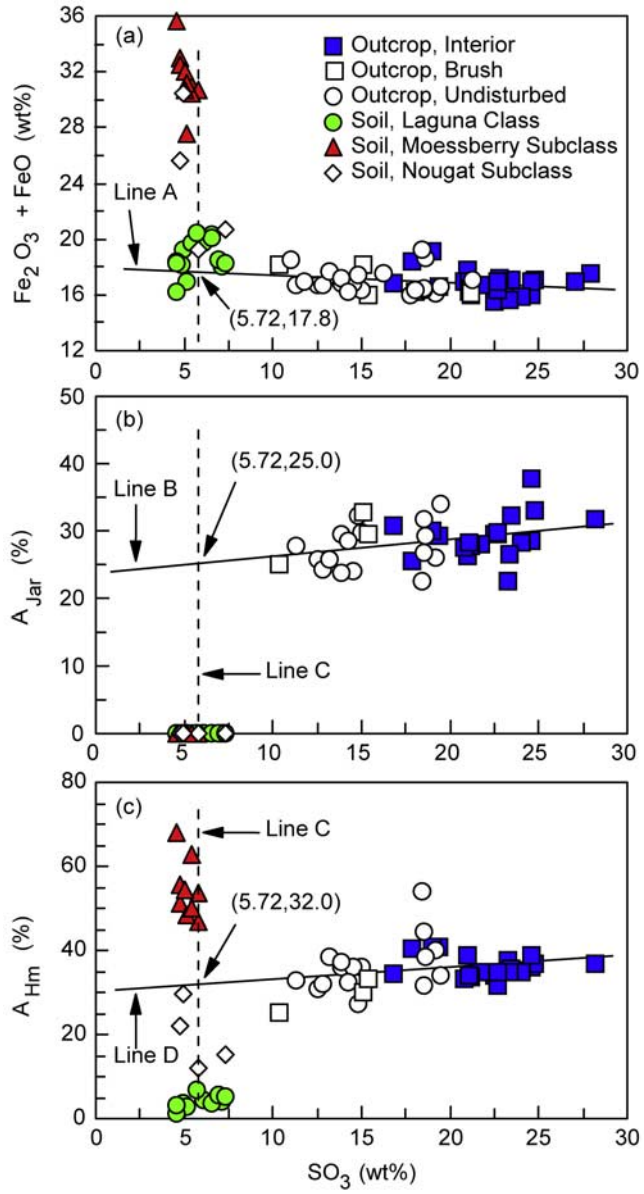

Figure 6. Plots of (a) Fe_2O_3 + FeO, (b) A_{Jar}, and (c) A_{Hm} versus SO_3 for outcrop and soil targets. The solid lines are linear least squares fits for outcrop data from undisturbed surfaces and surfaces exposed by brushing and grinding with the RAT. The dashed vertical line at SO_3 = 5.72 % is the average value of SO_3 for Laguna Class soil. The two lines intersect in the region defined by the Laguna Class soils in Figure 6a, showing that, with respect to APXS data, the analyses of undisturbed and brushed outcrop surfaces are on a mixing line between Laguna Class soil and "uncontaminated" outcrop exposed by RAT grinding. Plots in Figures 6b and 6c are parameters measured by MB (A_{Jar} and A_{Hm}) versus a parameter measured by APXS (SO_3), and the intersection of the two lines falls outside the region defined by the Laguna Class soil. This result shows that APXS data are more affected by thin soil and dust coatings than are MB data.

analyzed is laterally homogenous, the relevant parameter is the sampling depth, which is at least an order of magnitude deeper for MB relative to APXS. This difference is an important consideration in an environment such as Mars where thin alteration rinds and dusty surfaces are expected. A primary science rationale for the RAT was to remove thin dust coatings and rinds from rocks, permitting analysis of interior material [*Squyres et al.*, 2003].

[33] We investigate the relative sampling depths of the MB and APXS instruments in an empirical way in Figure 6 using data from Burns Outcrop Class, Laguna Class soil, and Berry Class soil (Table 4). In Figure 6a, we plot two parameters (Fe_2O_3 + FeO versus SO_3) that are both derived from APXS measurements. Interior rock outcrop surfaces exposed by the RAT are the closed square symbols and brushed and undisturbed surfaces are the open squares and circles, respectively. Extrapolation of the linear least squares fit of these data (line A) passes through the data for the Laguna Class soil. The straightforward interpretation of Figure 4a is that undisturbed outcrop surfaces are "contaminated" with Laguna Class soil and that grinding with the RAT exposed "clean" interior outcrop.

[34] In Figures 6b and 6c, we plot parameters measured by the MB (A_{Jar} and A_{Hm}) versus a parameter measured by the APXS instrument (SO_3). Again, we calculated linear least squares fits to the outcrop data (lines B and D). If the MB and APXS instruments sampled exactly the same material, extrapolation of lines B and D would pass through the data for Laguna Class soil, as in Figure 6a. However, lines B and D do not extrapolate through Laguna Class soil, a result that shows that the MB measurement sampled more of the outcrop and less of the contamination of Laguna Class soil than the APXS measurement. Unfortunately, we cannot quantify the thickness of the soil contamination or even whether it is continuous or discrete.

[35] The above discussion has implications for all observations and interpretations involving comparison of MB and APXS data for surfaces where grinding by the RAT cannot be done. For thin dust and/or soil coatings, the MB measurements will be relatively unaffected and the APXS measurements will be biased in the direction of the elemental composition of local dust or soil as just discussed above for the outcrop. Another example pertains to measurements of accumulations of spherules and their fragments. The maximum measured Fe concentration (Fe_2O_3 + FeO $\sim$ 35.6% (R. Gellert, manuscript in preparation, 2006)) and percentage of Fe from Hm (A_{Hm} = 68% from Table 3) for targets containing concentrations of spherules and their fragments are lower limits for the actual spherule Fe concentration and A_{Hm} value for two reasons. One is that the field of view of the APXS and MB instruments was never 100% occupied by spherules and their fragments, although it might be possible to correct for the portion of the field of view occupied by the spherules using MI images. The other reason is that it was not possible to remove dust coatings by brushing or grinding with the RAT. We discuss later an approach for inferring the elemental and mineralogical composition of spherules.

[36] A final example where the MB and APXS instruments are not seeing exactly the same sample, because of either lateral or sampling depth heterogeneities, is shown in Figure 6c. The Nougat Subclass soil has values of A_{Hm} that

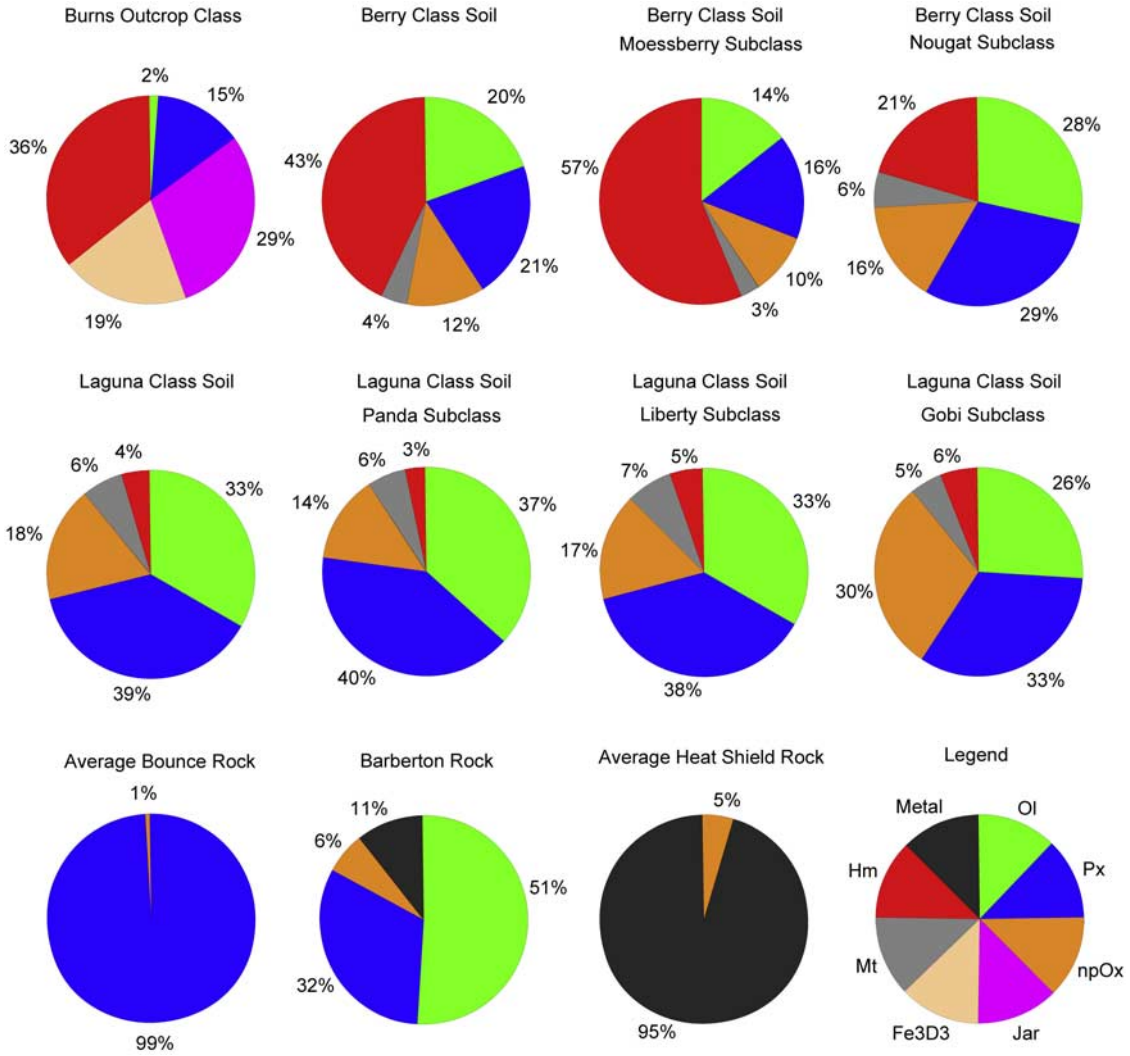

Figure 7. Pie diagrams showing the distribution of Fe in Fe-bearing phases for classes and subclasses of Meridian Planum soils and rocks. Laguna Class soil is also present at Gusev Crater.

are intermediate to those for the Laguna Class soil and the MoessBerry Subclass soil. On the basis of APXS data (Figure 6a), however, two Nougat Subclass soils have elemental abundances equivalent to Laguna Class soil and two have abundances similar to MoessBerry Subclass soil.

5. Mössbauer Mineralogy at Meridiani Planum

5.1. Elemental and Mineralogical Classification of Rock and Soil

[37] The surface of Meridiani Planum explored by the Opportunity rover can be described as a flat plain of S-rich outcrop that is mostly covered by thin surficial deposits of aeolian basaltic sand and dust, and lag deposits of hard Fe-rich spherules (and fragments thereof) that weathered from the outcrop and small unidentified rock fragments and cobbles [e.g., *Soderblom et al.*, 2004; *Squyres et al.*, 2006b; *Arvidson et al.*, 2006]. Surface expressions of the outcrop occur at impact craters (e.g., Eagle, Fram, Endurance, Erebus craters) and occasionally in troughs between ripple crests. In Table 4, we organized Meridiani Planum rocks and soil that were analyzed by MB into two rock classes (Burns Outcrop Class and Other Rocks Class) and two soil classes (Laguna Class with three subclasses and Berry Class with two subclasses). The Other Rocks Class is a collection of one-of-a-kind rocks (Bounce Rock, Heat Shield Rock, Barberton, and assorted cobbles [e.g., *Jolliff et al.*, 2006]). Laguna Class soil is the dominant soil at Gusev Crater [*Morris et al.*, 2006].

[38] The distribution of Fe in Fe-bearing phases in each class and subclass is shown as pie diagrams in Figure 7. The Burns Outcrop Class includes only analyses of interior surfaces that were exposed by RAT grinding. The S-rich outcrop has on average 29 ± 3% of Fe_T from jarosite, 36 ± 3% from hematite, 20 ± 2% from Fe3D3, and 14 ± 3% from pyroxene, and 2 ± 2% from olivine (Table 7). The Ol and Px are interpreted as undigested basaltic precursor of outcrop sediments. The observation of Px > Ol may reflect the relative abundance of those silicate phases in the precursor (Px > Ol), the relative susceptibility of the two phases to attack by acid-sulfate solutions (Ol > Px), or both. As

Table 7. Mössbauer Areas for Component Subspectra (f-Factor Corrected), Fe^{3+}/Fe_T, and Temperature Measurement Interval for Mössbauer Spectra of Classes and Subclasses of Meridiani Planum Rock and Soil

	Fe2D1 Ol, %	Fe2D2 Px, %	Fe3D1 npOx, %	Fe3D4 Jar, %	Fe3D3 Fe3D3, %	Mt, %	Fe3S1 Mt(3), %	Fe2.5S1 Mt(2.5), %	Fe3S2 Hm, %	Fe0S1 α-(Fe,Ni)^0, %	Sum, %	Fe^{3+}/Fe_T
Burns Outcrop Undisturbed Surfaces (All Locations)												
Average	4	14		28	19	0	0	0	35	0	100[a]	0.82
1σ	3[b]	4		4	3	0	0	0	4			0.06[c]
Burns Outcrop Surfaces Exposed by RAT Grinding (All Locations)												
Average	2	14	0	29	20	0	0	0	36	0	100	0.85
1σ	2	3	0	3	2	0	0	0	3			0.03
Burns Outcrop Surfaces Exposed by RAT Grinding (Eagle Crater)												
Average	1	12	0	29	21	0	0	0	38	0	100	0.87
1σ	2	3	0	8	4	0	0	0	2			0.03
Burns Outcrop Surfaces Exposed by RAT Grinding (Endurance Crater)												
Average	2	15	0	29	19	0	0	0	36	0	100	0.83
1σ	2	3	0	2	2	0	0	0	3			0.03
Burns Outcrop Surfaces Exposed by RAT Grinding (Plains)												
Average	1	9	0	32	21	0	0	0	36	0	100	0.90
1σ	2	2	0	2	2	0	0	0	2			0.03
Laguna Class Soil												
Average	33	38	18	0	0	6	2	4	4	0	100	0.27
1σ	5	4	8	0	0	2	2	2	2			0.08
Panda Subclass Soil												
Average	37	40	14	0	0	6	2	4	3	0	100	0.21
1σ	4	4	2	0	0	2	2	2	2			0.03
Liberty Subclass Soil												
Average	33	37	17	0	0	7	2	5	5	0	100	0.27
1σ	2	2	2	0	0	2	2	2	2			0.03
Gobi Subclass Soil												
Average	26	33	30	0	0	5	2	3	6	0	100	0.40
1σ	2	2	2	0	0	2	2	2	2			0.03
Berry Class Soil												
Average	20	22	12	0	0	4	2	2	42	0	100	0.57
1σ	9	7	6	0	0	3	2	2	20	0		0.15
MoessBerry Subclass Soil												
Average	14	16	10	0	0	3	1	2	56	0	100	0.68
1σ	3	3	3	0	0	3	2	2	7			0.06
Nougat Subclass Soil												
Average	29	29	16	0	0	6	3	3	21	0	100	0.40
1σ	6	3	7	0	0	3	2	2	8			0.06

[a]Because Mt = Mt(3) + Mt(2.5), Sum = Ol + Px + npOx + Jar + Fe3D3 + Mt + Hm + α-(Fe,Ni)^0.
[b]Uncertainty is 1σ of the average value or ±2% absolute, whichever is larger, for component subspectral area.
[c]Uncertainty is 1σ of the average value or ±0.03 units, whichever is larger, for Fe^{3+}/Fe_T.

discussed previously, the Hm analyzed in the outcrop occurs in the S-rock itself and not only from the embedded Hm-rich spherules. Jarosite and Fe3D3 were not detected as components of any soil.

[39] The difference between the Laguna and Berry Classes of soil is the degree of incorporation of the Hm-rich spherules and their fragments. The Laguna Class soils have 3–6% of Fe_T from Hm. This amount is only slightly more than that observed for Laguna Class soil at Gusev crater (2–3 %) [*Morris et al.*, 2006], and the difference may be related to a minor contribution of Hm from spherule fragments at Meridiani Planum. For comparable npOx concentrations, Laguna Class soil at Meridiani Planum has $A_{Px} > A_{Ol}$, which compares to $A_{Px} \sim A_{Ol}$ at Gusev crater, suggesting that the aggregate of basaltic source materials at Meridiani is more pyroxene rich (with respect to Fe mineralogy) than at Gusev crater. Because they have significant contributions from spherules and their fragments, the MoessBerry Subclass and Nougat Subclass of Berry Class soil have 56% and 21% of Fe_T from Hm, respectively. In fact, two soils from the MoessBerry Subclass (BerryBowl_MoessBerry and BerrySurvey_Cluster3) are concentrations of mostly whole spherules sitting on top of Laguna Class soil.

[40] The Other Rocks Class (Table 4 and Figure 7) is a collection of rocks whose elemental and/or Fe-mineralogical compositions are significantly different from other

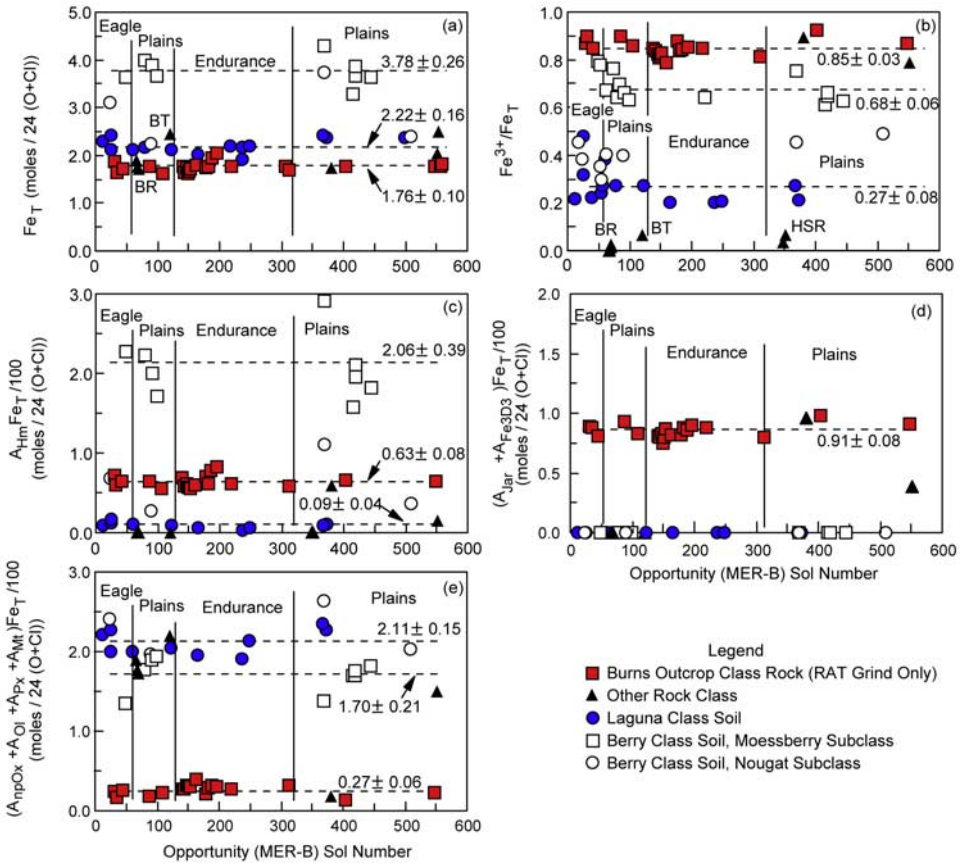

Figure 8. (a) Fe_T, (b) Fe^{3+}/Fe_T, (c) $A_{Hm}Fe_T/100$, (d) $(A_{Jar} + A_{Fe3D3})Fe_T/100$, and (e) $(A_{npOx} + A_{Ol} + A_{Px} + A_{Mt})Fe_T/100$ as a function of Opportunity sol number as a proxy for location. The solid vertical lines separate rover locations in Eagle crater, the plains east of Eagle crater to Endurance crater, Endurance crater, and the plains south of Endurance crater. Only interior surfaces of the Burns outcrop exposed by RAT grinding are plotted. The parameters $(A_{Jar} + A_{Fe3D3})Fe_T/100$ and $(A_{npOx} + A_{Ol} + A_{Px} + A_{Mt})Fe_T/100$ are good measures of the concentration of Fe associated with outcrop rock and basaltic soil, respectively. The horizontal dashed lines are average values for classes and subclasses of rocks. Numerical values are average ± 1σ. For Burns Outcrop Class, Laguna Class, MoessBerry Subclass, and Nougat Subclass, the plotted parameters do not have a significant dependence on location. BR, Bounce Rock; BT, Barberton Rock; HS, Heat Shield Rock.

surface materials at Meridiani Planum. Heat Shield Rock and Barberton have metallic Fe as a major component (95% and 11%, respectively) and are interpreted as meteorites [*Rodionov et al.*, 2005; *Schröder et al.*, 2006]. Bounce Rock is virtually monomineralogic Px with respect to Fe-bearing phases and is similar in chemical and mineralogical composition to a Martian meteorite found on Earth (EET79001, lithology B, and other basaltic shergottites) [*Rodionov et al.*, 2004; *Zipfel et al.*, 2004].

5.2. Mode of Occurrence of Surficial Deposits

5.2.1. Overview

[41] Surficial deposits of soil are present as thin (~1 m [*Soderblom et al.*, 2004]) and locally discontinuous cover over S-rich outcrop rocks, commonly forming aeolian bedforms, and as fill in places where the outcrop surface has been disrupted (e.g., by meteoritic impact). In Figure 8 we plot Fe_T from APXS measurements [*Rieder et al.*, 2004; R. Gellert, manuscript in preparation, 2006], the Fe^{3+}/Fe_T ratio, and the values of concentration of Fe associated with individual or multiple Fe-bearing phases (e.g., $A_{Hm}Fe_T/100$) as a function of Opportunity sol number as a proxy for location for the first 557 sols. Parameters having the form $A_{Hm}Fe_T/100$ are the percentage of Fe associated with a particular Fe-bearing phase (in this example Hm) from the MB experiment multiplied by Fe_T from the APXS experiment divided by 100 in units of moles/24(O + Cl). The units are expressed with respect to 24 anions because the number of oxygens in many common rock-forming minerals are factors of 24, for example olivine ($(Fe, Mg)_2SiO_4$), pyroxene ($(Fe, Mg, Ca)SiO_3$), magnetite (Fe_3O_4), and anorthite ($CaAl_2Si_2O_8$). For the outcrop, only analyses from surfaces exposed by RAT grinding are plotted. The parameters Fe_T, Fe^{3+}/Fe_T, $A_{Hm}Fe_T/100$, $(A_{Jar} + A_{Fe3D3})Fe_T/100$, and $(A_{npOx} + A_{Ol} + A_{Px} + A_{Mt})Fe_T/100$ have their maximum values for MoessBerry Subclass soil, Burns Outcrop Class rock, MoessBerry Subclass soil, Burns Outcrop Class rock, and Laguna Class soil, respectively. A general observation from Figure 8 is that the plotted parameters do not show a dependence on location for individual classes of samples.

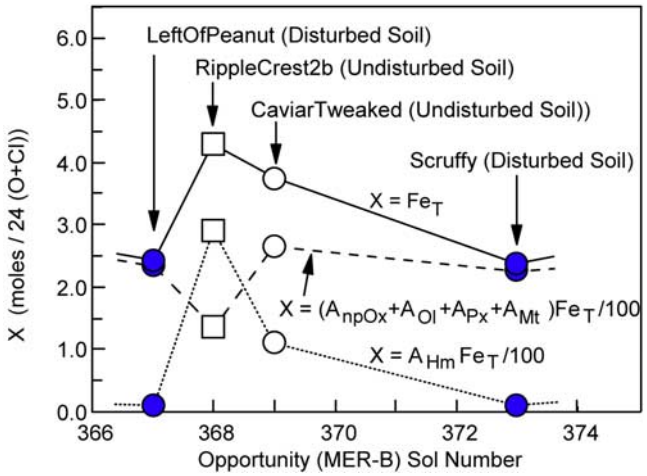

Figure 9. Plot of Fe_T, $A_{Hm}Fe_T/100$, and $(A_{npOx} + A_{Ol} + A_{Px} + A_{Mt})Fe_T/100$ versus sol number for a series of samples in and around a trench dug through a ripple on the plains south of Endurance crater. The subsurface is basaltic soil (LeftOfPeanut and Scruffy), the undisturbed surface of the ripple crest (RippleCrest2b) has high concentrations of Fe from hematite (spherules and their fragments), and the undisturbed surface downslope from the ripple crest (CaviarTweaked) is a mixture of basaltic soil and spherules, with the former dominant with respect to the total Fe concentration. The trench data show that hematite (from spherules and their fragments) is concentrated at the surface as a lag deposit.

Average and 1σ values are given in the figure for Burns Outcrop Class rock, Laguna Class soil, and MoessBerry Subclass soil.

5.2.2. Berry Class Soils

[42] Berry Class soils occur as surface lag deposits (MoessBerry and Nougat Subclasses) or as aggregates of mostly whole spherules on top of outcrop coated with a veneer of Laguna Class soil (MoessBerry Subclass). The Berry Class is widespread on the plains, and its occurrence as a surface lag at ripple crests was documented during sols 367–373 by analyses of soils near and in a trench made by the rover wheels that crosscut a ripple on the plains south of Endurance crater. In Figure 9, we plot Fe_T, $A_{Hm}Fe_T/100$, and $(A_{npOx} + A_{Ol} + A_{Px} + A_{Mt})Fe_T/100$ as a function of sol number. Sol 368 is the measurement of undisturbed soil on the ripple crest (MoessBerry Subclass), and it has the highest concentrations of both Fe_T and $A_{Hm}Fe_T/100$ from the accumulation of spherules and fragments thereof at the ripple crest. The other undisturbed soil at sol 369 (Nougat Subclass) was measured downslope from the ripple crest. Compared to the ripple crest, this soil has reduced contributions from spherules and their fragments and enhanced contributions from Laguna Class (basaltic) soil. The two disturbed soils at sols 367 (LeftOfPeanut) and 373 (Scruffy) have essentially no contribution from the spherules (Laguna Class), because $Fe_T \sim (A_{npOx} + A_{Ol} + A_{Px} + A_{Mt})Fe_T/100$. The LeftOfPeanut and Scruffy analyses were obtained from soil interior to the trench and a scuff mark made by the rover wheel. These two analyses and direct observation of the trench wall by the MI [*Arvidson et al.*, 2006] show that the Hm enrichment is confined to the very surface (i.e., a lag deposit). The ripple crest sample (RippleCrest2b) is enriched in Hm (i.e., spherules and their fragments) relative to the downslope sample (CaviarTweaked) because it is in a higher energy location with respect to the wind. The spherules and fragments thereof are expected to accumulate preferentially as lag particles relative to basaltic particles because they are the heaviest from density and size considerations (MI observations [e.g., *Arvidson et al.*, 2006; *Weitz et al.*, 2006]). The diameter of spherules and their fragments on ripple crests is 1.3–1.7 mm [*Weitz et al.*, 2006], and hematite and olivine, the most dense rock-forming silicate mineral, have bulk densities of ~5.2 and 3.2 g/cm^3, respectively [*Johnson and Olhoeft*, 1984]. The observation that the spherules and fragments thereof are the lag particles (rather than basaltic particles) does not prove they are solid hematite, but the observation is not inconsistent with the idea.

5.2.3. Laguna Class Soil

[43] As just discussed, Laguna Class soil on the plains is present as thin and locally discontinuous cover over outcrop rocks, commonly forming aeolian bedforms, and is armored

Table 8. Mössbauer Areas for Component Subspectra and Oxidation State for Martian Dust, Panda Subclass Soil, MoessBerry Subclass Soil, and Model Components

	Martian Dust			Panda Subclass		MoessBerry Subclass			
	GC,[a] %	MP,[b] %	Average Dust, %	GC,[c] %	MP,[c] %	Observed,[d] %	Spherule,[e] %	CBS1A,[f] %	CBS1B,[g] %
Ol	30 ± 2	28 ± 2	29 ± 2	39 ± 2	37 ± 4	14 ± 3	0	32 ± 7	33 ± 4
Px	33 ± 2	32 ± 2	32 ± 2	35 ± 2	40 ± 4	16 ± 3	0	36 ± 7	36 ± 4
npOx	28 ± 2	30 ± 2	29 ± 2	15 ± 1	14 ± 1	10 ± 3	0	22 ± 7	22 ± 2
Mt	7 ± 2	5 ± 2	6 ± 2	9 ± 2	6 ± 1	3 ± 3	0	7 ± 7	6 ± 2
Hm	2 ± 2	5 ± 2	3 ± 2	2 ± 2	3 ± 1	56 ± 7	100	3 ± 0	3 ± 2
Total	100	100	100	100	100	100	100	100	100
Fe^{3+}/Fe_T	0.36 ± 0.03	0.39 ± 0.03	0.38 ± 0.03	0.24 ± 0.02	0.21 ± 0.01	0.68 ± 0.06	1.00	0.28 ± 0.02	0.29 ± 0.02

[a]GC, Gusev crater. Analysis for soil Desert_Gobi [*Morris et al.*, 2006].
[b]MP, Meridiani Planum. Analysis for soil MountBlanc_LesHauches (Table 3).
[c]Data from *Morris et al.* [2006] and Table 7.
[d]Data from Table 7.
[e]Model spherule mineralogical composition.
[f]Calculated basaltic soil composition (CBS1A) from Observed = 0.55 × (Spherule) + 0.45 × (CBS1A).
[g]Calculated basaltic soil composition (CBS1B) from CBS1B = 0.50 × (Ave. Dust) + 0.50 × (MP Panda Subclass).

Table 9. Elemental Data for Martian Dust, Panda Subclass Soil, and MoessBerry Subclass Soil

	Martian Dust			Panda Subclass Soil		MoessBerry Subclass			
	GC,[a] %	MP,[a] %	Average,[b] %	GC,[c] %	MP,[c] %	Observed,[c] %	Spherule,[d] %	CBS2A,[e] %	CBS2B,[f] %
SiO_2	44.71 ± 0.52	44.97 ± 0.29	44.84 ± 0.52	46.52 ± 0.57	46.78 ± 1.22	38.54 ± 1.10	0.00	45.69 ± 1.32	45.81 ± 1.19
TiO_2	0.89 ± 0.08	1.01 ± 0.07	0.95 ± 0.08	0.87 ± 0.15	1.02 ± 0.18	0.73 ± 0.05	0.00	0.86 ± 0.06	0.99 ± 0.17
Al_2O_3	9.49 ± 0.16	9.14 ± 0.09	9.32 ± 0.18	10.46 ± 0.71	9.67 ± 0.49	7.63 ± 0.23	0.00	9.05 ± 0.28	9.50±0.46
Cr_2O_3	0.31 ± 0.04	0.32 ± 0.03	0.32 ± 0.04	0.36 ± 0.08	0.41 ± 0.08	0.28 ± 0.03	0.00	0.33 ± 0.04	0.37 ± 0.04
Fe_2O_3	6.58 ± 0.07	7.97 ± 0.03	7.28 ± 0.70	4.20 ± 0.54	4.36 ± 0.74	20.24 ± 4.37	99.70	5.62 ± 0.97	5.82 ± 0.98
FeO	10.52 ± 0.11	10.31 ± 0.04	10.42 ± 0.11	12.18 ± 0.57	13.75 ± 1.00	11.17 ± 3.55	0.00	13.24 ± 4.26	12.09 ± 0.88
MnO	0.31 ± 0.02	0.34 ± 0.01	0.33 ± 0.02	0.33 ± 0.02	0.38 ± 0.02	0.28 ± 0.02	0.00	0.34 ± 0.02	0.36±0.02
MgO	8.20 ± 0.15	7.57 ± 0.08	7.89 ± 0.32	8.93 ± 0.45	7.31 ± 0.30	6.55 ± 0.25	0.00	7.76 ± 0.30	7.60 ± 0.31
CaO	6.13 ± 0.07	6.54 ± 0.04	6.34 ± 0.20	6.27 ± 0.23	7.12 ± 0.28	5.23 ± 0.37	0.00	6.20 ± 0.44	6.73 ± 0.26
Na_2O	2.89 ± 0.29	2.22 ± 0.19	2.56 ± 0.33	3.02 ± 0.37	2.23 ± 0.23	2.16 ± 0.11	0.00	2.56 ± 0.13	2.40 ± 0.25
K_2O	0.48 ± 0.07	0.48 ± 0.06	0.48 ± 0.07	0.41 ± 0.03	0.49 ± 0.07	0.38 ± 0.03	0.00	0.45 ± 0.04	0.49 ± 0.07
P_2O_5	0.90 ± 0.09	0.93 ± 0.07	0.92 ± 0.09	0.83 ± 0.23	0.82 ± 0.05	0.81 ± 0.04	0.00	0.96 ± 0.05	0.87 ± 0.05
SO_3	7.56 ± 0.13	7.28 ± 0.07	7.42 ± 0.13	4.90 ± 0.74	4.97 ± 0.58	5.17 ± 0.42	0.00	6.13 ± 0.50	6.20 ± 0.72
Cl	0.88 ± 0.03	0.78 ± 0.01	0.83 ± 0.05	0.61 ± 0.08	0.57 ± 0.06	0.69 ± 0.03	0.00	0.81 ± 0.04	0.70 ± 0.07
Br ($x10^4$)	29 ± 22	26 ± 14	28 ± 22	49 ± 12	39 ± 27	56 ± 22	0	66 ± 26	34 ± 24
Ni ($x10^4$)	636 ± 73	467 ± 42	552 ± 85	544 ± 159	399 ± 100	854 ± 182	3000	479 ± 106	476 ± 119
Zn ($x10^4$)	406 ± 32	401 ± 14	404 ± 32	204 ± 71	238 ± 63	329 ± 25	0	391 ± 30	321 ± 85
Total	99.85	99.87	99.86	99.89	99.89	99.84	100.00	100.00	99.88
Fe^{3+}/Fe_T	0.36 ± 0.03	0.41 ± 0.03	0.39 ± 0.03	0.24 ± 0.02	0.22 ± 0.03	0.66 ± 0.06	1.00	0.28 ± 0.02	0.30 ± 0.02

[a]GC, Gusev crater; MP, Meridiani Planum. Analyses of Desert_Gobi and MontBlanc_LesHauches are from *Gellert et al.* [2006a,b].
[b]Uncertainty is larger of deviation from average value and maximum value for analytical uncertainty.
[c]Data are average $\pm 1\sigma$ of data from *Gellert et al.* [2006] and R. Gellert (manuscript in preparation, 2006).
[d]Model spherule elemental composition.
[e]Calculated composition of basaltic soil (CBS2A) from Observed = 0.16 × (Spherule) + 0.84 × (CBS2A). In this calculation, the spherules account for ~50% of the total Fe.
[f]Calculated composition of basaltic soil (CBS2B) from CBS2B = 0.50 × (Ave. Dust) + 0.50 × (MP Panda Subclass).

by a thin veneer (lag deposit) of MoessBerry Subclass soil. This relationship is present at trench sites studied during sols 23–26 (Eagle crater), 78–80 (plains between Eagle and Endurance craters), 367–373 (plains south of Endurance crater). By direct MI observations, Laguna Class soil at Meridiani Planum has spherules dispersed throughout, but spherule number density is low and none was included in the MB (and APXS) measurements. Surface expressions of undisturbed Laguna Class soils are generally found in association with impact craters (e.g., MontBlanc_LesHauches, Millstone_Dahlia, and Auk_AukRAT; Table 4).

[44] Because it has the highest proportion of npOx, the Gobi Subclass of Laguna Class soil is the most representative of global Martian dust. The soil Desert_Gobi at Gusev crater is a bright, undisturbed soil. There are three Gobi Subclass soils at Meridiani Planum (Table 4). One of them (MontBlanc_LesHauches) is undisturbed soil that occurs on the downwind lip of Eagle crater. It is bright, fine-grained material (dust) deposited in the wind eddy created by the lip of the crater [*Soderblom et al.*, 2004; *Yen et al.*, 2005].

5.3. Mineralogical and Elemental Composition of Global Martian Dust

[45] Bright, undisturbed soils Desert_Gobi (Gusev crater) and MontBlanc_LesHauches (Meridiani Planum), from opposite sides of the planet, have among the highest concentrations of npOx and are thus our current best analyses of global aeolian dust. Their individual and average Fe-mineralogical and elemental compositions are given in Tables 8 and 9, respectively. Between the two soils, there is no significant difference in Fe-mineralogical composition and there are only minor differences in the elemental composition. Mineralogical observations of dust from Martian orbit by the Mars Global Surveyor Thermal Emission Spectrometer [*Bandfield and Smith*, 2003] and the Martian surface by the MER MiniTES [*Christensen et al.*, 2004a] are consistent with the presence of plagioclase feldspar [*Bandfield et al.*, 2003], although *Ruff* [2004] has suggested zeolite instead. Visible, near-IR (VNIR) observations of dust from Martian orbit by OMEGA show a ferric absorption edge (presumably from npOx) and no detectable evidence for spectral features near 1.4, 1.9, and 2.1–2.6 μm that would be indicative of molecular H_2O and M-OH (M = Si, Al, Mg, and Fe) functional groups [*Bibring et al.*, 2006]. The VNIR observations imply the absence of phyllosilicate (and zeolite) minerals in the dust and constrain npOx away from forms that have high concentrations of H_2O (e.g., ferrihydrite) and OH-bearing phases that have weak spectral features 2.1–2.6 μm because of poor crystallinity or formation of strong hydrogen bonds (e.g., FeOOH polymorphs). Mössbauer spectra of dust collected by MER magnets are interpreted by an assemblage of olivine, pyroxene, magnetite, and npOx as the Fe-bearing phases [*Goetz et al.*, 2005]. On the basis of observations made during the Mars Pathfinder mission, mean particle diameter of Martian dust is 3.4 ± 0.6 μm [*Markiewicz et al.*, 1999]. For MER, the mean particle diameters are 2.94 ± 0.42 μm and 3.04 ± 0.36 μm at Gusev crater and Meridiani Planum, respectively [*Lemmon et al.*, 2004]. Other estimates range from 0.2 to 10 μm [e.g., *Murphy et al.*, 1993; *Pollack et al.*, 1995].

[46] Bright Martian dust can therefore be described as an assemblage of particles in the clay plus fine silt size range (<5 μm) that contain primary igneous minerals (olivine, pyroxene, feldspar, and magnetite) and sulfate-bearing alteration/weathering products (npOx but not phyllosilicate minerals). Discrete dust particles are predominately compo-

sites of these phases rather than predominantly monophase [e.g., *Madsen et al.*, 1999; *Goetz et al.*, 2005]. The strongly magnetic mineral in the dust (and Laguna Class soil in general) is magnetite [*Morris et al.*, 2004, 2006; *Goetz et al.*, 2005].

5.4. Mineralogical and Elemental Compositions of Spherules (Blueberries)

[47] As discussed above and previously reported [*Klingelhöfer et al.*, 2004; *Christensen et al.*, 2004b], observations by the MER MB and MiniTES instruments firmly establish that the spherules (the so-called "blueberries") and their fragments have hematite as an important mineralogical component. Unfortunately, it has not been possible to obtain MB and APXS analyses on surface targets that are wholly spherules. The maximum values of A_{Hm} and Fe_2O_3 + FeO for a spherule-rich soil are 68% and 35.6%, respectively, for TrenchRipple_RippleCrest2b (Table 3 and R. Gellert (manuscript in preparation, 2006)). In comparison, average Meridiani Planum Laguna Class soil has $A_{Hm} = 4 \pm 2$ % and Fe_2O_3 + FeO = 18.9 ± 1.3 % (Table 7 and calculated from R. Gellert (manuscript in preparation, 2006)). The lower limit for the hematite content of the spherules is 24% on the basis of the following two assumptions: (1) soil TrenchRipple_RippleCrest2b, which actually has $A_{Hm} = 68\%$, is entirely spherules (i.e., $A_{Hm} = 100\%$), so that its elemental composition is the bulk spherule composition, and (2) the hematite is stoichiometric Fe_2O_3. Note that, although all spherules presumably have their origin in the S-rich outcrop, they do not have detectable Jar or Fe3D3 as Fe-mineralogical components. We discuss next an upper limit estimate.

[48] In principle, it is possible to estimate the relative proportions of spherules and basaltic soil in the field of view of both instruments from MI images and use this information and the mineralogical and elemental compositions of basaltic soil to calculate the corresponding compositions of the spherules. This approach was taken by *Jolliff and the Athena Science Team* [2005], working with APXS data, and they concluded that the spherules might contain 45–60 wt.% as Fe_2O_3. However, this calculation is not straightforward, because (as also noted by *Jolliff and the Athena Science Team* [2005]) the surface being analyzed is not flat. Spherules are rounded and, because of their size (2.9 ± 1.2 mm for unfractured spherules [*Weitz et al.*, 2006]) protrude from the surface. An additional complication is that there are at least two populations of basaltic materials: one is relatively coarse-grained basaltic soil which is intermixed with spherules and the other is a thin layer of dust coating all particles. To avoid these issues, we adopted a different approach.

[49] Table 8 has four columns under MoessBerry Subclass. The first is the observed average Fe-mineralogical composition. The second is a limiting Fe-mineralogical composition for the Fe spherules that we wish to test, namely $A_{Hm} = 100\%$. In the third column, we mathematically backed out the composition of the basaltic soil (CBS1A) that would have to be mixed with the spherule composition to give the observed composition in column one. The constraint for the calculation was $A_{Hm} = 3\%$ for the basaltic soil, which is the average value for Martian dust and Meridiani Planum Panda Subclass soil. With this constraint for the basaltic soil and the constraint of $A_{Hm} = 100\%$ for the spherules, average MoessBerry Subclass soil is 45% CBS1A and 55% spherule with respect to Fe-bearing phases.

[50] Is CBS1A a reasonable Fe-mineralogical composition for a basaltic soil? Panda Subclass is the subclass of Laguna Class soil with the least npOx (i.e., least dust component), so that average Martian dust and this soil subclass (columns four and six in Table 8, respectively) are end-members for Meridiani Planum soils. The last column in Table 8 (CBS1B) was calculated for a mixture of 50% average Martian dust and 50% Meridiani Planum Panda Subclass soil. The calculated Fe-mineralogical compositions CBS1A and CBS1B are nearly identical. This correspondence shows that the constraint $A_{Hm} = 100\%$ is viable, so that the spherules can be entirely hematite with respect to their Fe-mineralogical composition.

[51] The calculations just described for MB data were repeated for APXS elemental data, and the corresponding four columns of data for MoessBerry Subclass are shown in Table 9. With the spherule composition set to 100 % Fe_2O_3, a calculated soil composition was obtained using 16% and 84% for the percentages of spherule and basaltic soil, respectively. Those percentages were chosen because they gave ~5.6 % Fe_2O_3 in the calculated composition, a value that is intermediate between dust and Panda Subclass soil at Meridiani Planum (Table 9). The calculated composition is consistent with the elemental composition of basaltic soils, except for Ni which is too high at ~1013 μg/g. After adjusting the spherule composition to include a Ni impurity, possibly present as a co-precipitate with the hematite [*Yen et al.*, 2006], we calculated the basaltic soil composition CBS2A in Table 9.

[52] Is CBS2A a reasonable elemental composition for Meridiani Planum basaltic soil? Using the same procedure developed above for calculating CBS1B, we calculated the last column of Table 9 as the CBS2B composition using 50% average Martian dust and 50% Meridiani Planum Panda Subclass soil. The calculated elemental compositions CBS2A and CBS2B are nearly identical. This result shows that the spherules can be ~100% Fe_2O_3 with respect to their elemental composition.

[53] Summarizing, MB and APXS data show that the hematite content of the spherules is between 24 and 100%. It may seem inconsistent that the calculations use very different spherule percentages for the MB and APXS calculations (55% and 16%, respectively). However, this is not the comparison to make, because the percentages are not both calculated with respect to Fe contents. For elemental data, the spherules account for ~50% of the total Fe, a percentage in good agreement with the MB value. As discussed by *Christensen et al.* [2004b] and *Calvin et al.* [2006], MiniTES spectra, which unlike MB are sensitive to the entire ensemble of mineralogical components, are also consistent with the spherule mineralogical composition being dominated by hematite.

5.5. Fe-Mineralogical Stratigraphy of the Burns Formation

[54] The stratigraphy of the Burns formation, primarily as observed at Endurance crater, is discussed in detail by *Grotzinger et al.* [2005]. They defined three major units

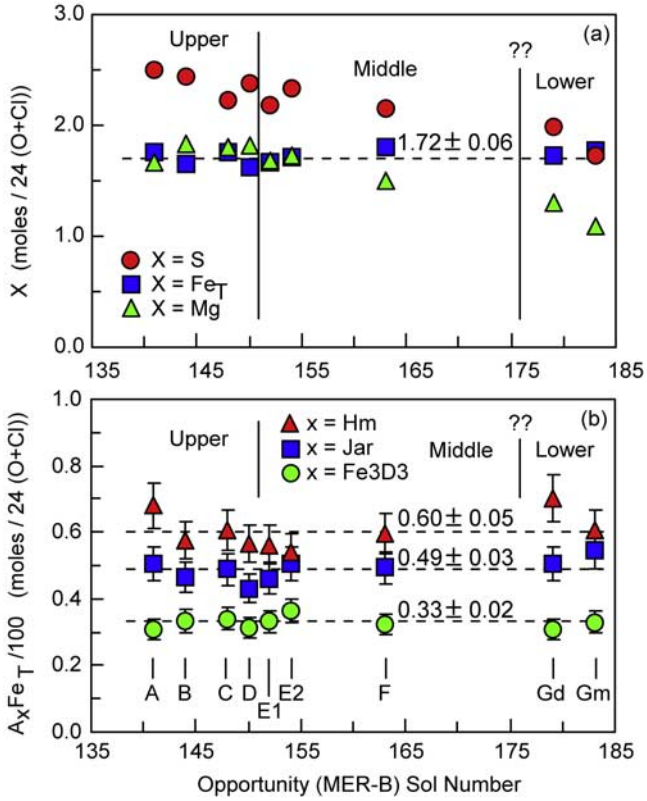

Figure 10. Stratigraphy of the Burns formation at Endurance crater for (a) molar concentrations of Fe_T, S, and Mg and (b) molar concentrations of Fe from Hm, Jar, and Fe3D3. Increasing Opportunity sol number corresponds to downsection, and the unit designations are from *Grotzinger et al.* [2005]. The horizontal dashed lines are the average ± 1σ values for Fe_T in Figure 10a and $A_{Hm}Fe_T$/100, $A_{Jar}Fe_T$/100, and $A_{Fe3D3}Fe_T$/100 in Figure 10b. Fe_T and the concentrations of Fe from Hm, Jar, and Fe3D3 show no detectable stratigraphic variations.

on the basis of sedimentologic and diagenetic characteristics. The lower, middle, and upper units are interpreted to represent eolian dune field, eolian sand sheet, and mixed eolian sand sheet and interdune facies associations, respectively, with local evidence for subaqueous flow in the upper unit. The authors argue that the Burns formation records, from lower to upper units, a progressive influence of water in controlling depositional processes. The stratigraphic section was sampled by grinding with the RAT at nine locations in Endurance crater during sols 140–183 [*Squyres and Knoll*, 2005]. Locations A, B, C, and D are in the upper unit, E1, E2, and F are in the middle unit, and Gd and Gm are imprecisely located in the region of the bottom of the middle unit or the top of the lower unit [*Grotzinger et al.,* 2005].

[55] APXS and MB data for the stratigraphic section in Endurance crater are shown in Figure 10. Fe_T is constant throughout the section (1.72 ± 0.06 moles/24(O + Cl)), S systematically decreases, and Mg is constant in the middle and upper units and decreases in the lower unit. Si and Al (not shown) increase as S and Mg decrease [*Clark et al.*, 2005]. The concentrations of Fe associated with hematite, jarosite, and Fe3D3 are constant through the section (average ± 1σ = 0.60 ± 0.05, 0.49 ± 0.03, and 0.33 ± 0.02 moles/24(O + Cl), respectively). In fact, these concentrations are constant for all outcrop surfaces exposed by RAT grinding (average ± 1σ = 0.63 ± 0.08, 0.51 ± 0.06, and 0.34 ± 0.04 moles/24(O + Cl), respectively) at Meridiani. Note that the concentration of Fe associated with Hm is derived predominantly if not wholly from the sulfate-rich matrix rock and not the spherules. Apparently, the concentrations of the Fe-bearing phases were essentially invariant with respect to location during the formation of outcrop rock and remained invariant through subsequent diagenetic processes.

[56] The invariance of the concentrations of Fe from Hm, Jar, and Fe3D3 and the relatively constant elemental chemistry suggest alteration of precursor materials that was approximately isochemical with respect to elements other than S and Cl. Basaltic soil is a candidate precursor material, for example. Panda Subclass soil from the opposite side of the planet (Gusev crater) has the same elemental composition (on a SO_3- and Cl-free basis) as Panda Subclass soil at Meridiani Planum for all elements at the 2σ level, and for all elements except CaO and MgO at the 1σ level (Table 10). Martian dust also has the same elemental composition to within 2σ. Thus it is not unreasonable to have a precursor of basaltic soil for the outcrop that is relatively homogenous with respect to elemental composition.

[57] The last column in Table 10 is the calculated elemental composition for the basaltic precursor of the Burns formation (OCBP1) with respect to SO_3 = Cl = 0 and assuming isochemical alteration. It was calculated from the average composition for outcrop surfaces exposed by RAT grinding [*Rieder et al.*, 2004; R. Gellert, manuscript in preparation, 2006] and Fe^{3+}/Fe_T = 0.23, which is the average value for Panda Subclass soil. Like the Panda Subclass soils, the OCBP1 composition is basaltic, but it has higher concentrations of Fe_2O_3+FeO, MgO, K_2O, and P_2O_5 and lower concentrations of Al_2O_3, Cr_2O_3, and Na_2O. The OCBP1 composition is a window to the past, giving a possible elemental composition of the materials in the source region of the Meridiani Planum sediments before they were altered and deposited to form the Burns formation.

6. Mineralogical Evidence for Aqueous, Acid-Sulfate Processes

[58] The MER Mössbauer spectrometers provide information about aqueous process on Mars through the detection of Fe-bearing minerals that contain H_2O or OH in their structure and/or are the products of aqueous activity. At Gusev crater, goethite (α-FeOOH) was detected as a mineralogical marker for aqueous processes in rocks of the Columbia Hills [*Morris et al.*, 2006]. At Meridiani Planum, jarosite within the Burns formation is a mineralogical marker for aqueous processes because it contains the equivalent of ~10 wt. % H_2O in its structure as the OH anion. Using average outcrop values of A_{Jar} ~ 29 % (Table 7) and (Fe_2O_3 + FeO) ~ 17%, we calculate that average outcrop has the equivalent of ~2% H_2O associated with just the jarosite. *Clark et al.* [2005] infer from mineralogical models of the outcrop that 6–20% equivalent H_2O could be present in the outcrop. In contrast to Gusev

Table 10. Elemental Data for Gusev Crater and Meridiani Planum Panda Subclass Soil, Average Martian Dust, and Outcrop Precursor Basalt Calculated to a SO_3- and Cl-free Composition

	GC Panda Subclass,[a] %	MP Panda Subclass,[a] %	Average Dust,[a] %	OCBP1,[b] %
SiO_2	49.23 ± 0.32	49.53 ± 1.12	48.86 ± 0.32	48.19 ± 1.61
TiO_2	0.92 ± 0.16	1.08 ± 0.02	1.04 ± 0.08	1.01 ± 0.05
Al_2O_3	11.07 ± 0.67	10.24 ± 0.49	10.15 ± 0.10	8.06 ± 0.41
Cr_2O_3	0.38 ± 0.09	0.43 ± 0.09	0.35 ± 0.04	0.25 ± 0.02
Fe_2O_3	4.44 ± 0.59	4.62 ± 0.78	7.93 ± 0.76	5.08
FeO	12.90 ± 0.68	14.56 ± 1.13	11.35 ± 0.12	15.67 ± 1.02
MnO	0.35 ± 0.03	0.40 ± 0.02	0.36 ± 0.02	0.43 ± 0.05
MgO	9.45 ± 0.49	7.74 ± 0.31	8.60 ± 0.35	10.40 ± 1.55
CaO	6.64 ± 0.22	7.54 ± 0.29	6.91 ± 0.22	6.46 ± 0.61
Na_2O	3.20 ± 0.38	2.36 ± 0.24	2.79 ± 0.36	2.19 ± 0.19
K_2O	0.43 ± 0.03	0.52 ± 0.07	0.52 ± 0.08	0.75 ± 0.04
P_2O_5	0.88 ± 0.24	0.87 ± 0.05	1.00 ± 0.10	1.37 ± 0.07
SO_3	0.00	0.00	0.00	0.00
Cl	0.00	0.00	0.00	0.00
Br ($x10^4$)	52 ± 13	42 ± 29	31 ± 24	107 ± 144
Ni ($x10^4$)	576 ± 169	423 ± 104	601 ± 93	798 ± 118
Zn ($x10^4$)	216 ± 77	252 ± 68	440 ± 35	554 ± 126
Total	99.89	99.89	99.86	99.87
Fe^{3+}/Fe_T	0.24 ± 0.02	0.22 ± 0.03	0.39 ± 0.04	0.23

[a]Calculated from elemental data in Table 9.
[b]Calculated composition of outcrop basaltic precursor (OCBP1) from elemental data (R. Gellert, manuscript in preparation, 2006) for outcrop surfaces exposed by RAT grinding, $Fe^{3+}/Fe_T = 0.23$, and $SO_3 = Cl = 0$.

crater where goethite is a component in rocks whose regional volumetric extent is not known, the Burns formation is laterally extensive ($\sim 10^5$ km^2 [*Christensen et al.*, 2001]), thick (~600 m [*Hynek et al.*, 2002]), and the probable source of the ~7% equivalent H_2O identified by the Odyssey orbiter for the Meridiani Planum region [*Feldman et al.*, 2004].

[59] An important aspect of the jarosite detection is that acidic conditions (pH < 4 at room temperature [e.g., *Dutrizac and Jambor*, 2000; *Stoffregen et al.*, 2000]) are required for its formation. Hydrothermal conditions permit jarosite precipitation at very low pH (pH = 1–2 at ~100°C) and also promote hematite over goethite as the jarosite hydrolysis product [*Stoffregen et al.*, 2000]. The observation of both hematite and jarosite and the absence of definitive goethite detection in the sulfate-rich outcrop by MB suggest that the initial alteration of basaltic precursor material may have taken place under hydrothermal conditions.

[60] Because jarosite, hematite, and $Fe(SO_4)(OH)$ form a triple point under hydrothermal conditions [*Stoffregen et al.*, 2000], the unassigned Fe3D3 doublet is possibly superparamagnetic hematite or $Fe(SO_4)(OH)$, although the MB parameters of the later are not known to us. The alteration of basaltic precursor material (possibly soil) under oxidizing, acid-sulfate conditions to form jarosite and other phases could have occurred under conditions provided, for example, by interactions with acid-sulfate (possibly hydrothermal) waters [*Burns*, 1988; *Burns and Fisher*, 1990; *McLennan et al.*, 2005] and/or condensation of SO_2-rich volcanic emanations [*Clark and Baird*, 1979; *Settle*, 1979; *Banin et al.*, 1997].

7. Summary

[61] Mössbauer mineralogy (Fe^{3+}/Fe_T, identification of Fe-bearing phases, and the distribution of Fe among Fe-bearing phases) was done on 95 rock and soil targets by Opportunity during its first 557 sols of roving on Meridiani Planum. Salient results and interpretations are summarized next.

[62] 1. The oxidation state of Fe ranged from Fe^{3+}/Fe_T = 0.00 to 0.93. The least oxidized targets ($Fe^{3+}/Fe_T \leq 0.06$) are isolated rocks (BounceRock, Barberton, and Heat Shield rock). Values of Fe^{3+}/Fe_T for Laguna Class (basaltic) soil and Berry Class (Hm-rich) soils average 0.27 ± 0.08 and 0.57 ± 0.15, respectively. Surfaces of S-rich outcrop rocks of the Burns formation exposed by RAT grinding are very oxidized with average $Fe^{3+}/Fe_T = 0.85 \pm 0.03$.

[63] 2. Eight Fe-bearing phases were identified: kamacite as a Fe^0-bearing phase, Ol and Px as Fe^{2+}-bearing phases, Mt as a Fe^{2+}- and Fe^{3+}-bearing phase, and npOx, Hm, jarosite, and Fe3D3 as Fe^{3+}-bearing phases. On the basis of chemistry and Fe-mineralogical composition, Meridian Planum rock and soil are grouped into two rock and two soil classes: Burns Class outcrop, other rock class, Laguna Class soil (with Panda, Liberty, and Gobi Subclasses) and Berry Class soil (with Nougat and MoessBerry Subclasses).

[64] 3. Ol, Px, npOx, and minor Mt and Hm are the Fe-bearing phases in Laguna Class soil. The same Fe-bearing phases are also present in Berry Class soil, but Hm is the major Fe-mineralogical component. The two Fe^0-bearing rocks (Barberton and Heat Shield rock) are interpreted as meteorites. BounceRock, essentially monomineralic Px for Fe-bearing phases, is interpreted as an impact erratic.

[65] 4. Laguna Class soil is present as thin and locally discontinuous cover over outcrop rocks, commonly forming aeolian bedforms. MoessBerry Subclass soils are present as accumulations of Hm-rich spherules on outcrop surfaces and as lag deposits at ripple crests.

[66] 5. The average elemental and Fe-mineralogical compositions of global Martian dust is approximated by the average of corresponding compositions of Gobi Subclass soils MontBlanc_LesHauches (Meridiani Planum) and

Desert_Gobi (Gusev crater). The mineralogical composition of Martian dust is primarily npOx plus primary igneous phases (Ol, Px, Mt, and, from TES data, plagioclase feldspar).

[67] 6. The S-rich rock of Burns Outcrop Class is Jar, Hm, Fe3D3, and minor Px and Ol. This mineralogical composition pertains to the S-rich rock and does not include a contribution from spherules (blueberries). The exact Fe-mineralogical and elemental compositions of the spherules are not known but are constrained between 24–100% Hm. The spherules do not have detectable contributions from Jar and Fe3D3.

[68] 7. A stratigraphic section of the Burns formation was examined at Endurance crater. The molar concentrations of Fe associated with Jar, Fe3D3, and Hm in the outcrop are invariant across this section. On a S- and Cl-free basis (S = Cl = 0), the Burns formation has a basaltic bulk composition that is enriched in Fe_2O_3+FeO, MgO, K_2O, and P_2O_5 and depleted in Al_2O_3, Cr_2O_3, and Na_2O compared to Laguna Class soil.

[69] 8. The presence of jarosite is mineralogical evidence for the presence of H_2O/OH on Mars and for acid-sulfate aqueous processes.

[70] **Acknowledgments.** R.V.M., D.W.M., and D.W.M. acknowledge support of the NASA Mars Exploration Rover Project and the NASA Johnson Space Center. Development of the MIMOS II Mössbauer spectrometer was funded by the German Space Agency under contract 50QM 99022 and supported by the Technical University of Darmstadt and the University of Mainz. Part of the work described in this paper was conducted at the Jet Propulsion Laboratory, California Institute of Technology, under a contract with the National Aeronautics and Space Administration. P.A.deS. acknowledges support of CAPES (contract PASJ 142/1999) and CVRD from Brazil. The support of the Russian Space agency is acknowledged. We acknowledge the unwavering support of JPL engineering and MER operations staff and the MER Athena Science Team. We thank D. Agresti, A. Wang, F. Berry, and B. Jolliff for detailed and thoughtful reviews of the manuscript.

References

Arvidson, R. E., et al. (2006), Nature and origin of the hematite-bearing plains of Terra Meridiani based on analyses of orbital and Mars Exploration rover data sets, *J. Geophys. Res.*, *111*, E12S08, doi:10.1029/2006JE002728.

Bandfield, J. L., and M. D. Smith (2003), Multiple emission angle surface-atmosphere separations of Thermal Emission Spectrometer data, *Icarus*, *161*, 47–65.

Bandfield, J. L., T. D. Glotch, and P. R. Christensen (2003), Spectroscopic identification of carbonate minerals in the Martian dust, *Science*, *301*, 1084–1087.

Banin, A., F. X. Han, I. Kan, and A. Cicelsky (1997), Acidic volatiles and the Mars soil, *J. Geophys. Res.*, *102*, 13,341–13,356.

Bibring, J.-P., et al. (2006), Global mineralogical and aqueous Mars history derived from OMEGA/Mars Express data, *Science*, *312*, 400–404.

Bishop, J. L., H. Froschl, and R. L. Mancinelli (1998), Alteration processes in volcanic soils and identification of exobiologically important weathering products on Mars using remote sensing, *J. Geophys. Res.*, *103*, 31,457–31,476.

Burns, R. G. (1986), Terrestrial analogues of the surface rocks of Mars?, *Nature*, *320*, 55–56.

Burns, R. G. (1987), Ferric sulfates on Mars, *Proc. Lunar Planet. Sci. Conf. 17th*, Part 2, *J. Geophys. Res.*, *92*, suppl., E570–E574.

Burns, R. G. (1988), Gossans on Mars, *Proc. Lunar Planet. Sci. Conf. 18th*, 713–721.

Burns, R. G. (1993), Rates and mechanisms of chemical weathering of ferromagnesian silicate minerals on Mars, *Geochim. Cosmochim. Acta*, *57*, 4555–4574.

Burns, R. G., and D. S. Fisher (1990), Evolution of sulfide mineralization on Mars, *J. Geophys. Res.*, *95*, 14,169–14,173.

Burns, R. G., and T. C. Solberg (1990), ^{57}Fe-bearing oxide, silicate, and aluminosilicate minerals, crystal structure trends in Mossbauer spectra, in *Spectroscopic Characterization of Minerals and Their Surfaces*, pp. 262–283, Am. Chem. Soc., Washington, D. C.

Calvin, W. M., T. D. Glotch, R. E. Arvidson, S. Wiseman, J. R. Johnson, S. W. Ruff, A. T. Knudson, and P. R. Christensen (2006), Directional emissivity effects on the Meridiani plains, *Lunar Planet. Sci.* [CD-ROM], *XXXVII*, Abstract 1481.

Christensen, P. R., R. V. Morris, M. D. Lane, J. L. Bandfield, and M. C. Malin (2001), Global mapping of Martian hematite mineral deposits: Remnants of water-driven processes on early Mars, *J. Geophys. Res.*, *106*, 23,873–23,885.

Christensen, P. R., et al. (2004), Initial results from the Mini-TES experiment in Gusev crater from the Spirit rover, *Science*, *305*, 837–842.

Christensen, P. R., et al. (2004), Mineralogy at Meridiani Planum from the Mini-TES experiment on the Opportunity rover, *Science*, *306*, 1733–1739.

Clark, B. C., and A. K. Baird (1979), Is the Martian lithosphere sulfur rich?, *J. Geophys. Res.*, *84*, 8395–8403.

Clark, B. C., et al. (2005), Chemistry and mineralogy of outcrops at Meridiani Planum, *Earth. Planet. Sci. Lett.*, *240*, 73–94.

Dang, M.-Z., D. G. Rancourt, J. E. Dutrizac, G. Lamarche, and R. Provencher (1998), Interplay of surface conditions, particle size, stoichiometry, cell parameters, and magnetism in synthetic hematite-like minerals, *Hyperfine Interact.*, *117*, 271–319.

De Grave, E., and A. Van Alboom (1991), Evaluation of ferrous and ferric Mossbauer fractions, *Phys. Chem. Miner.*, *18*, 337–342.

De Grave, E., and R. E. Vandenberghe (1990), Mossbauer effect study of the spin structure in natural hematites, *Phys. Chem. Miner.*, *17*, 344–352.

de Souza, P. A., Jr. (1999), Automation in Mössbauer spectroscopy analysis, *Lab. Robot. Autom.*, *11*, 13–23.

Dutrizac, J. E., and J. L. Jambor (2000), Jarosites and their application in hydrometallurgy, in *Sulfate Minerals: Crystallography, Geochemistry, and Environmental Significance*, *Rev. Mineral. Geochem.*, vol. 40, edited by C. N. Alpers, J. L. Jambor, and D. K. Nordstom, pp. 454–479, Mineral. Soc. of Am., Washington, D. C.

Dyar, M. D., and M. W. Schaefer (2004), Mossbauer spectroscopy on the surface of Mars: Constraints and expectations, *Earth Planet. Sci. Lett.*, *218*, 243–259.

Feldman, W. C., et al. (2004), Global distribution of near-surface hydrogen on Mars, *J. Geophys. Res.*, *109*, E09006, doi:10.1029/2003JE002160.

Fernandez-Remolar, D. C., R. V. Morris, J. E. Gruener, R. Amils, and A. H. Knoll (2005), The Rio Tinto Basin, Spain: Mineralogy, sedimentary geobiology, and implications for interpretation of outcrop rocks at Meridiani Planum, Mars, *Earth Planet. Sci. Lett.*, *240*, 149–167.

Gellert, R., et al. (2006), Alpha Particle X-Ray Spectrometer (APXS): Results from Gusev crater and calibration report, *J. Geophys. Res.*, *111*, E02S05, doi:10.1029/2005JE002555.

Goetz, W., et al. (2005), Indication of drier periods on Mars from the chemistry and mineralogy of atmospheric dust, *Nature*, *436*, 62–65, doi:10.1038/nature03807.

Greenwood, N. N., and T. C. Gibb (1971), *Mossbauer Spectroscopy*, CRC Press, Boca Raton, Fla.

Grotzinger, J. P., et al. (2005), Stratigraphy and sedimentology of a dry to wet eolian depositional system, Burns formation, Meridiani Planum, Mars, *Nature*, *240*, 11–72.

Gütlich, P., R. F. Link, and A. Trautwein (1978), *Mössbauer Spectroscopy and Transition Metal Chemistry*, Springer, New York.

Herbert, R. B., Jr. (1997), Properties of goethite and jarosite precipitated from acidic groundwater, Dalarna, Sweden, *Clays Clay Minerals*, *45*, 261–273.

Hrynkiewicz, A. Z., J. Kubisz, and D. S. Kulgawczuk (1965), Quadrupole splitting of the 14.4 gamma line of ^{57}Fe in iron sulfates of the jarosite group, *J. Inorg. Nucl. Chem.*, *27*, 2513–2517.

Hynek, B. M., R. E. Arvidson, and R. J. Phillips (2002), Geologic setting and origin of Terra Meridiani hematite deposit on Mars, *J. Geophys. Res.*, *107*(E10), 5088, doi:10.1029/2002JE001891.

Johnson, G. R., and G. R. Olhoeft (1984), Densities of rocks and minerals, in *CRC Handbook of Physical Properties of Rocks*, vol. III, edited by R. S. Carmichael, pp. 1–38, CRC Press, Boca Raton, Fla.

Johnson, J. H. (1977), Jarosite and akaganeite from White Island volcano, New Zealand: An X-ray and Mossbauer study, *Geochim. Cosmochim. Acta*, *41*, 539–544.

Jolliff, B. L., and the Athena Science Team (2005), Composition of Meridiani hematite-rich spherules: A mass-balance mixing model approach, *Lunar Planet. Sci.*, *XXXVI*, Abstract 2269.

Jolliff, B. L., W. H. Farrand, J. R. Johnson, C. Schröder, C. M. Weitz, and the Athena Science Team (2006), Origin of rocks and cobbles on the Meridiani plains as seen by Opportunity, *Lunar Planet. Sci.*, *XXXVII*, Abstract 2401.

Klingelhöfer, G., et al. (2003), Athena MIMOS II Mössbauer spectrometer investigation, *J. Geophys. Res.*, *108*(E12), 8067, doi:10.1029/2003JE002138.

Klingelhöfer, G., et al. (2004), Jarosite and hematite at Meridiani Planum from Opportunity's Mossbauer spectrometer, *Science*, *306*, 1740–1745.

Leclerc, A. (1980), Room temperature Mössbauer analysis of jarosite-type compounds, *Phys. Chem. Miner.*, *6*, 327–334.
Lemmon, M. T., et al. (2004), Atmospheric imaging results from the Mars Exploration Rovers: Spirit and Opportunity, *Science*, *306*, 1753–1756.
Madsen, M. B., S. F. Hviid, H. P. Gunnlaugsson, J. M. Knudsen, W. Goetz, C. T. Pedersen, A. R. Dinesen, C. T. Mogensen, M. Olsen, and R. B. Hargraves (1999), The magnetic properties experiments on Mars Pathfinder, *J. Geophys. Res.*, *104*, 8761–8779.
Markiewicz, W. J., R. M. Sablotny, H. U. Keller, N. Thomas, D. Titov, and P. Smith (1999), Optical properties of the Martian aerosols derived from Imager for Mars Pathfinder midday sky brightness data, *J. Geophys. Res.*, *104*, 9009–9017.
McCammon, C. (1995), Mossbauer spectroscopy of minerals, in *Mineral Physics and Crystallography: A Handbook of Physical Constants*, *AGU Ref. Shelf*, vol. 2, edited by T. J. Ahrens, pp. 332–347, AGU, Washington, D. C.
McLennan, S. M., et al. (2005), Provenance and diagenesis of the evaporite-bearing Burns formation, Meridiani Planum, Mars, *Earth Planet. Sci. Lett.*, *240*, 95–121.
Ming, D. W., et al. (2006), Geochemical and mineralogical indicators for aqueous processes in the Columbia Hills of Gusev crater, Mars, *J. Geophys. Res.*, *111*, E02S12, doi:10.1029/2005JE002560.
Morris, R. V., H. V. Lauer Jr., C. A. Lawson, E. K. Gibson Jr., G. A. Nace, and C. Stewart (1985), Spectral and other physicochemical properties of submicron powders of hematite (α-Fe_2O_3), maghemite (γ-Fe_2O_3), magnetite (Fe_3O_4), goethite (α-FeOOH), and lepidocrocite (γ-FeOOH), *J. Geophys. Res.*, *90*, 3126–3144.
Morris, R. V., D. C. Golden, J. F. Bell III, and H. V. Lauer Jr. (1995), Hematite, pyroxene, and phyllosilicates on Mars: Implications from oxidized impact melt rocks from Manicouagan Crater, Quebec, Canada, *J. Geophys. Res.*, *100*, 5319–5328.
Morris, R. V., D. W. Ming, D. C. Golden, and J. F. Bell III (1996), An occurrence of jarositic tephra on Mauna Kea, Hawaii: Implications for the ferric mineralogy of the Martian surface, in *Mineral Spectroscopy: A Tribute to Roger G. Burns*, edited by M. D. Dyar, C. McCammon, and M. W. Schaefer, *Spec. Publ. Geochem. Soc.*, *5*, 327–336.
Morris, R. V., et al. (2000), Mineralogy, composition, and alteration of Mars Pathfinder rocks and soils: Evidence from multispectral, elemental, and magnetic data on terrestrial analogue, SNC meteorite, and Pathfinder samples, *J. Geophys. Res.*, *105*, 1757–1817.
Morris, R. V., et al. (2004), Mineralogy at Gusev Crater from the Mössbauer spectrometer on the Spirit rover, *Science*, *305*, 833–836.
Morris, R. V., et al. (2006), Mössbauer mineralogy of rock, soil, and dust at Gusev crater, Mars: Spirit's journey through weakly altered olivine basalt on the plains and pervasively altered basalt in the Columbia Hills, *J. Geophys. Res.*, *111*, E02S13, doi:10.1029/2005JE002584.
Murad, E., and J. H. Johnston (1987), Iron oxides and oxyhydroxides, in *Mossbauer Spectroscopy Applied to Inorganic Chemistry*, vol. 2, edited by G. J. Long, pp. 507–582, Springer, New York.
Murphy, J. R., R. M. Haberle, O. B. Toon, and J. B. Pollack (1993), Martian global dust storms: Zonally symmetric numerical simulations including size-dependent particle transport, *J. Geophys. Res.*, *98*, 3197–3220.
Pollack, J. B., M. E. Ockert-Bell, and M. K. Shepard (1995), Viking lander image analysis of Martian atmospheric dust, *J. Geophys. Res*, *100*, 5235–5250.
Rieder, R., R. Gellert, J. Brückner, G. Klingelhöfer, G. Dreibus, A. Yen, and S. W. Squyres (2003), The new Athena alpha particle X-ray spectrometer for the Mars Exploration Rovers, *J. Geophys. Res.*, *108*(E12), 8066, doi:10.1029/2003JE002150.
Rieder, R., et al. (2004), Chemistry of rocks and soils at Meridiani Planum from the Alpha Particle X-ray Spectrometer, *Science*, *306*, 1746–1749.
Rodionov, D., et al. (2004), Mössbauer investigation of 'Bounce rock' at Meridiani Planum on Mars—Indications for the first shergottite on Mars, *Meteorit. Planet. Sci.*, *39*(NR8), suppl., A91.
Rodionov, D. S., G. Klingelhoefer, D. W. Ming, R. V. Morris, C. Schröder, P. A. de Souza, S. W. Squyres, and A. S. Yen (2005), An iron-nickel meteorite on Meridiani Planum: Observations by MER Opportunity's Moessbauer spectrometer, in *Geophysical Research Abstracts, 7, Abstracts of the Contributions of the EGU General Assembly 2005, Vienna, Austria, 24–29 April 2005*, Abstract EGU05-A-10242, Eur. Geosci. Union, Strasbourg, France.
Ruff, S. W. (2004), Spectral evidence for zeolite in the dust on Mars, *Icarus*, *168*, 131–143.
Schröder, C., et al. (2006), A stony meteorite discovered by the Mars Exploration Rover Opportunity on Meridiani Planum, Mars, *Meteorit. Planet. Sci.*, *41*, suppl., 5285.
Settle, M. (1979), Formation and deposition of volcanic sulfate aerosols on Mars, *J. Geophys. Res.*, *84*, 8343–8354.
Soderblom, L. A., et al. (2004), Soils of Eagle Crater and Meridiani Planum at the Opportunity Rover landing site, *Science*, *306*, 1723–1726.
Squyres, S. W., and A. H. Knoll (2005), Sedimentary rocks at Meridiani Planum: Origin, diagenesis and implications for life on Mars, *Earth Planet. Sci. Lett.*, *240*, 1–10.
Squyres, S. W., et al. (2003), Athena Mars rover science investigation, *J. Geophys. Res.*, *108*(E12), 8062, doi:10.1029/2003JE002121.
Squyres, S. W., et al. (2004), The Opportunity rover's Athena science investigation at Meridiani Planum, Mars, *Science*, *306*, 1698–1703.
Squyres, S. W., et al. (2006a), Rocks of the Columbia Hills, *J. Geophys. Res.*, *111*, E02S11, doi:10.1029/2005JE002562.
Squyres, S. W., et al. (2006b), Overview of the Opportunity Mars Exploration Rover Mission to Meridiani Planum: Eagle Crater to Purgatory Ripple, *J. Geophys. Res.*, *111*, E12S12, doi:10.1029/2006JE002771.
Stevens, J. G., A. M. Khasanov, J. W. Miller, H. Pollak, and Z. Li (1998), *Mössbauer Mineral Handbook*, Biltmore, Ashville, N. C.
Stoffregen, R. E., C. N. Alpers, and J. L. Jambor (2000), Alunite-jarosite crystallography, thermodynamics, and geochemistry, in *Sulfate Minerals: Crystallography, Geochemistry, and Environmental Significance*, *Rev. Mineral. Geochem.*, vol. 40, edited by C. N. Alpers, J. L. Jambor, and D. K. Nordstom, pp. 453–480, Mineral. Soc. of Am., Washington, D. C.
Weitz, C. M., R. C. Anderson, J. F. Bell III, W. H. Farrand, K. E. Herkenhoff, J. R. Johnson, B. L. Jolliff, R. V. Morris, S. W. Squyres, and R. J. Sullivan (2006), Soil grain analyses at Meridiani Planum, Mars, *J. Geophys. Res.*, *111*, E12S04, doi:10.1029/2005JE002541.
Yen, A. S., et al. (2005), An integrated view of the chemistry and mineralogy of Martian soils, *Nature*, *436*, 49–54, doi:10.1038/nature03637.
Yen, A. S., et al. (2006), Nickel on Mars: Constraints on meteoritic material at the surface, *J. Geophys. Res.*, *111*, E12S11, doi:10.1029/2006JE002797.
Zipfel, J., et al. (2004), APXS analyses of Bounce Rock—The first basaltic shergottite on Mars, *Meteorit. Planet. Sci.*, *39*(NR8), suppl., A118.

R. E. Arvidson, Department Earth and Planetary Sciences, Washington University, St. Louis, MO 63130, USA.
B. Bernhardt, P. A. de Souza Jr., J. Foh, P. Gütlich, I. Fleischer, G. Klingelhöfer, F. Renz, C. Schröder, and D. S. Rodionov, Institut für Anorganische und Analytische Chemie, Johannes Gutenberg-Universität, D-55099 Mainz, Germany.
U. Bonnes and E. Kankeleit, Darmstadt University of Technology, D-64289 Darmstadt, Germany.
B. A. Cohen, Institute of Meteoritics, University of New Mexico, Albuquerque, NM 87131, USA.
E. N. Evlanov and B. Zubkov, Space Research Institute IKI, 117997 Moscow, Russia.
R. Gellert, Department of Physics, University of Guelph, Guelph, ON, Canada N1G 2W1.
T. McCoy and M. E. Schmidt, Department of Mineral Sciences, National Museum of Natural History, Smithsonian Institution, 10th and Constitution Avenue, NW, Washington, DC 20560-0119, USA.
D. W. Ming, D. W. Mittlefehldt, and R. V. Morris, NASA Johnson Space Center, Mail Code KR, Houston, TX 77058, USA. (richard.v.morris@nasa.gov)
S. W. Squyres, Department of Astronomy, Cornell University, 428 Space Sciences Building, Ithaca, NY 14853, USA.
T. Wdowiak, Department of Physics, University of Alabama at Birmingham, Birmingham, AL 35294, USA.
A. Yen, Jet Propulsion Laboratory, California Institute of Technology, Pasadena, CA 91109, USA.